Molecular and topological reorganizations in mitochondrial architecture interplay during Bax-mediated steps of apoptosis

Nicholas R. Ader[1,2], Patrick C. Hoffmann[1], Iva Ganeva[1], Alicia C. Borgeaud[1], Chunxin Wang[2], Richard J. Youle[2], Wanda Kukulski[1,*]

[1]Cell Biology Division, MRC Laboratory of Molecular Biology, Cambridge, CB2 0QH UK.

[2]Biochemistry Section, Surgical Neurology Branch, National Institutes of Neurological Disorders and Stroke, National Institutes of Health, Bethesda, MD 20892, USA.

*Corresponding author – kukulski@mrc-lmb.cam.ac.uk

ABSTRACT

During apoptosis, Bcl-2 proteins such as Bax and Bak mediate the release of pro-apoptotic proteins from the mitochondria by clustering on the outer mitochondrial membrane and thereby permeabilizing it. However, it remains unclear how outer membrane openings form. Here, we combined different correlative microscopy and electron cryo-tomography approaches to visualize the effects of Bax activity on mitochondria in human cells. Our data show that Bax clusters localize near outer membrane ruptures of highly variable size. Bax clusters contain structural elements suggesting a higher-order organization of their components. Furthermore, unfolding of inner membrane cristae is coupled to changes in the supramolecular assembly of ATP synthases, particularly pronounced at membrane segments exposed to the cytosol by ruptures. Based on our results, we propose a comprehensive model in which molecular reorganizations of the inner membrane and sequestration of outer membrane components into Bax clusters interplay in the formation of outer membrane ruptures.

INTRODUCTION

Controlled cell death mediated by the mitochondria is a critical check on inappropriate cell proliferation (Labi and Erlacher, 2015; Youle and Strasser, 2008). Pro-apoptotic members of the Bcl-2 protein family, including Bax, Bak, and the less studied Bok, are central to facilitating the necessary release of apoptotic factors, such as cytochrome *c* and Smac/DIABLO, from the mitochondria into the cytosol (Jürgensmeier et al., 1998; Ke et al., 2018). In healthy cells, Bax cycles between the surface of mitochondria and the cytosol, while Bak resides mostly on mitochondria (Edlich et al., 2011; Griffiths et al., 1999). Upon activation by apoptotic stimuli, Bax/Bak stably inserts into the outer membrane of the mitochondria. This step leads to permeabilization of the outer membrane, which is required for release of the apoptotic factors from the intermembrane space, the compartment formed from the intracristal and peripheral space (Lovell et al., 2008).

Bax has been long known to form membrane pores and ruptures *in vitro* (Antonsson et al., 1997; Basañez et al., 1999; Schafer et al., 2009; Schlesinger et al., 1997). Visual evidence for outer membrane ruptures in mitochondria of intact cultured cells has only been obtained recently. Super-resolution fluorescence microscopy (FM) revealed that activated Bax forms rings devoid of outer mitochondrial membrane proteins, that were suggested to correspond to outer membrane ruptures several hundreds of nm in diameter (Grosse et al., 2016; Salvador-Gallego et al., 2016). The occurrence of such large ruptures has been confirmed by electron cryo-tomography

(cryo-ET), and associated with the extrusion of mitochondrial DNA (mtDNA) through the opened outer membrane (McArthur et al., 2018).

While the mechanism of formation of these large ruptures remains elusive, the ability of Bax/Bak to associate into clusters appears to be essential for permeabilizing the outer membrane (Antonsson et al., 2000; Nechushtan et al., 2001; Westphal et al., 2014). The conformational changes that lead to Bax activation include insertion of a transmembrane helix into the outer membrane and subsequent dimerization of membrane-bound Bax (Bleicken et al., 2014; Brouwer et al., 2014; Czabotar et al., 2013; Dewson et al., 2008; Dewson et al., 2012). Further accumulation into larger Bax/Bak assemblies involves interactions via multiple, labile interfaces (Uren et al., 2017). In FM, the formation of these assemblies can be observed as small punctae on the mitochondria that coalescence into larger, mitochondria-associated cytosolic clusters that contain thousands of Bax/Bak molecules (Nasu et al., 2016; Nechushtan et al., 2001; Zhou and Chang, 2008). It is only poorly understood how the initial association of Bax/Bak molecules within the planar membrane rearranges into a three-dimensional cluster (Uren et al., 2017). Further, the mechanism by which formation of large clusters contributes to the release of apoptotic factors is not clear.

In addition to outer membrane rupturing, activation of Bax/Bak has been implicated in inner mitochondrial membrane rearrangements, suggested to be required for efficient discharge of apoptotic factors trapped in the intracristal space (Ban-Ishihara et al., 2013; Cipolat et al., 2006; Frezza et al., 2006; Scorrano et al., 2002). The

relationship between changes in inner membrane morphology, the formation of large outer membrane ruptures, and cytosolic Bax/Bak clusters is unclear.

Here, we used a set of correlative microscopy approaches, including electron tomography (ET) of resin-embedded as well as vitreous cells, to visualize the cellular structures associated with signals of GFP-tagged Bax. We thereby investigated membrane rupturing, cluster formation and inner membrane remodeling at high resolution. Our data suggest that these Bax-mediated events interplay to facilitate the release of apoptotic factors.

RESULTS

Bax clusters form regions of ribosome-exclusion in the cytosol

To mimic Bax-mediated apoptosis in HeLa cells, we took advantage of the previous observation that overexpression of Bax can induce cell death by apoptosis (Han et al., 1996; Pastorino et al., 1998). When cells expressed cytosolic GFP-Bax in the presence of the caspase inhibitor Q-VD-OPh, we observed on average 77 minutes later (SD 70 min, N=86 cells) that GFP-Bax translocated to the mitochondria, which displayed fragmentation typical for apoptosis, as expected (Karbowski et al., 2002; Fig. 1A and B). On average, 102 minutes (SD 57 min, N=92 cells) after the initial recruitment into diffraction-limited punctae (Fig. 1B), larger, irregular clusters of Bax appeared (Fig. 1C). Cells representing these two stages were similarly frequent 14 - 18 h after GFP-Bax transfection. We confirmed by immunofluorescence that partial release of cytochrome *c* occurred upon formation of initial Bax foci, and became more pronounced

when larger Bax clusters appeared (Suppl. Fig. S1). Consequently, for our further experiments, we chose 16 h after GFP-Bax transfection as a time point that captures stages around cytochrome *c* release.

To visualize Bax clusters and associated mitochondrial membrane shape, we imaged resin-embedded cells by correlative FM and ET (Ader and Kukulski, 2017; Kukulski et al., 2011) (Fig. 2). We targeted 82 GFP-Bax signals by ET, and found that 79 of them localized adjacent to mitochondria (Fig. 2; *crosses*). Further, of the 82 GFP-Bax signals imaged, 77 localized to dense regions in the cytosol that were devoid of other cytosolic features. In particular, they excluded the otherwise ubiquitously distributed ribosomes (Fig. 2). These regions were irregular in shape and extended over approximately 100 to 1300 nm. More intense GFP-Bax signals corresponded to larger ribosome-exclusion zones (Fig. 2F). We thus conclude that these ribosome-exclusion zones in the cytosol correspond to the Bax clusters previously observed by immuno-electron, fluorescence and super-resolution microscopy (Grosse et al., 2016; Nasu et al., 2016; Nechushtan et al., 2001; Salvador-Gallego et al., 2016; Zhou and Chang, 2008).

Mitochondria near Bax clusters display outer membrane ruptures, influx of cytosolic content, and inner membrane restructuring

The mitochondria that we found near GFP-Bax clusters often exhibited substantial gaps in their outer membranes (Fig. 2), which we henceforth refer to as ruptures. These ruptures were between 100 and 700 nm wide (mean 317 nm, SD 159

115 nm, N=37). Of the 37 mitochondrial ruptures we found, 33 directly bordered the Bax
116 clusters (Fig. 2). Near the rupture, the remaining outer membrane appeared associated
117 with the inner membrane at a similar distance as in non-ruptured regions. There were
118 no outer membrane segments peeling off significantly from the inner membrane, or
119 membrane segments loosely adhering to the remaining outer membrane. Although most
120 ruptured mitochondria had single ruptures visible, occasionally two ruptures could be
121 discerned at different regions of the same mitochondrion.

122 In twelve of the ruptured mitochondria, we observed ribosome-like structures,
123 often several dozen, in the intermembrane space (Fig. 2F and J; *red circles and white*
124 *spheres*). In electron tomograms, ribosomes are easy to recognize because of the their
125 dense staining and ubiquitous presence in the cytosol (Watson, 1958). As mitochondrial
126 ribosomes are confined to the mitochondrial matrix, we concluded that these were
127 ribosomes that had leaked in from the cytosol through the outer membrane rupture. We
128 also found 62 mitochondria near GFP-Bax clusters that had ribosomes in the
129 intermembrane space, but that had no outer membrane ruptures visible within the
130 tomogram (Fig. 2H and L; *red circles and white spheres*). The ribosomes in the
131 intermembrane space suggested that many of the mitochondria we imaged had
132 ruptures that were not contained within the imaged cell volume. Therefore, the presence
133 of ribosomes in the intermembrane space offered indirect confirmation of outer
134 membrane rupture, and indicated a relocation of cytosolic content into the
135 intermembrane space upon outer membrane rupturing.

The ruptured mitochondria in our dataset showed a wide heterogeneity of inner membrane morphology. While some ruptured mitochondria displayed canonical cristae folding (Fig. 2E), others lacked cristae over large areas of a smooth inner membrane (Fig. 2G and H). Furthermore, we frequently observed more than one inner membrane compartment surrounded by a single outer membrane, indicating fragmentation of the inner membrane without concomitant outer membrane fission. In these cases, one matrix displayed canonical cristae shape, while the other matrix lacked cristae (Fig. 2F). These observations indicate that, besides outer membrane ruptures, Bax activity induces fragmentation and restructuring of the inner membrane.

Drug-induced apoptosis has similar effects on both outer and inner membrane to Bax overexpression

We next set out to test whether the mitochondrial restructurings we observed in HeLa cells upon overexpression of Bax were general hallmarks of intrinsic apoptosis. We therefore analyzed Bax/Bak double knockout (DKO) HCT116 cells stably expressing GFP-Bax, in which we induced apoptosis with ABT-737, a BH3 mimetic pro-apoptotic compound (van Delft et al., 2006) (Supp. Fig. S2). We found that the signals of GFP-Bax foci localized to ribosome-exclusion zones like in HeLa cells overexpressing GFP-Bax (Supp. Fig. S2G). We also observed ruptured outer membranes, mostly (3 of 5 ruptures) near Bax clusters. The ruptures were, however, less frequent (5 ruptures for 41 GFP-Bax target signals) than in HeLa cells. These ruptured mitochondria displayed multiple matrices and unfolded inner membranes,

158 similar to those in Bax-overexpressing HeLa cells (Supp. Fig. S3D-L). Furthermore, 13
159 other mitochondria had multiple matrices, while no rupture was observed within the
160 imaged cell volume. These results suggest that ribosome-excluding Bax clusters,
161 ruptures in the outer membrane, as well as rearrangements of the inner membrane are
162 characteristic of Bax activity independent of means inducing apoptosis.
163
164 **Bax clusters consist of a sponge-like meshwork**
165 We next sought to obtain higher resolution details of Bax cluster organization by
166 using cryo-ET. In tomograms of resin-embedded cells, the clusters appeared
167 amorphous (Fig. 2), but protein structures are best preserved in vitreous ice (Dubochet
168 et al., 1988). We therefore used a correlative cryo-microscopy approach that allowed us
169 to locate GFP-Bax clusters in vitreous sections of HeLa cells that were vitrified by high-
170 pressure freezing (Bharat et al., 2018) (Fig. 3A, B, E, and F). In electron cryo-
171 tomograms acquired at the predicted GFP-Bax locations, we found ribosome-exclusion
172 zones in the cytosol, in agreement with our data from resin-embedded cells (Fig. 3C
173 and G) (N=7 GFP-Bax signals). Within these exclusion zones, we could discern
174 ultrastructural details that were not visible in the electron tomograms of resin-embedded
175 cells (Fig. 3D and H, and Movies 1 and 2). We found irregularly arranged plane and line
176 segments that appeared to be part of a dense network within the Bax cluster (Fig. 3D'
177 and H', and Movies 1 and 2; *red highlights*). These data suggest that Bax clusters are
178 not amorphous, featureless structures, but that they contain elements indicative of a
179 higher-order ultrastructural organization.

While vitreous sections allow precise localization of fluorescent signals to electron cryo-tomograms (Bharat et al., 2018), artifacts induced by the sectioning process limit interpretability of structural details (Al-Amoudi et al., 2005). We therefore moved on to thinning cells grown on EM grids and vitrified by plunge-freezing using cryo-focused ion beam (FIB) milling (Mahamid et al., 2016; Marko et al., 2007). Prior to cryo-FIB milling, we screened these grids by cryo-FM to identify target cells that were transfected with GFP-Bax and were at the stage of Bax cluster formation. Furthermore, by targeting cell regions containing GFP-Bax clusters (Suppl. Fig. S3A-F), we increased the likelihood that the clusters were contained in the thin lamellae produced by cryo-FIB milling (Suppl. Fig. S3G-L). We then collected electron cryo-tomograms of mitochondria visibly identified in intermediate magnification maps of the lamellae (Fig. 3I and L). Adjacent to outer mitochondrial membrane ruptures in three different cells, we found 6 ribosome-exclusion zones that contained similar structural motifs as observed in vitreous sections. We therefore attributed these regions to correspond to Bax clusters (Fig. 3K, N and Q; Movies 3 and 4). These regions contained small planar segments, which manifest as lines in individual tomographic slices. The segments appeared irregularly connected to each other in a network (Fig. 3K', N' and Q' and Movies 3 and 4; *red highlights*). The average length of the segments was 21 nm, SD 5.6 nm (N=59 segments from 3 clusters found in 2 cells). In addition, dot-like densities could be discerned at and between the segments (Fig. 3K', N' and Q'; Movies 3 and 4; *red highlights*). The network ultrastructure resembled a sponge with irregular fenestration, containing patches of high or low density.

Thus, using two different vitrification and two independent imaging methods, we identify structural motifs that suggest that Bax clusters are higher-order structures and their supramolecular organization resembles a sponge-like meshwork.

Inner membrane flattening is most definite at outer membrane ruptures and inner membrane reshaping correlates with rupture size

We sought to use the superior preservation in cryo-ET to reveal details of the changes in membrane architecture occurring to apoptotic mitochondria. First, we inspected the ruptures in the outer mitochondrial membranes from 5 cells (Fig. 3 I-Q and Fig. 4). The ruptured membrane bilayers displayed distinct, often sharp edges (Fig. 4, D-I) that were similar in thickness to the rest of the membrane. Some of the rupture edges appeared embedded into the cluster (Fig. 3K, N, Q and Fig. 4D-F, H). Furthermore, fragments of the bilayer that were continuous with the outer membrane appeared also connected to the cluster (Fig. 3Q, yellow arrowheads). In 10 of the 11 outer membrane ruptures we visualized by cryo-ET, the inner membrane appeared intact with no visible rupture. In only one case, we observed that both outer and inner membrane were ruptured, and a Bax cluster was protruding through the rupture into the mitochondrial matrix (Fig. 3O-Q'). In the other cases, at the site of outer membrane rupture, substantial segments of the inner membrane were exposed to the cytosol (Fig. 4A-C). These membrane segments contained no membrane protrusions or folds reminiscent of cristae. Thus, these segments appeared very smooth relative to the rest

of the inner membrane, which displayed cristae of variable curvature that protruded into the matrix (Fig. 4J-L).

We classified the ruptured mitochondria that we observed, both by ET of resin-embedded cells and by cryo-ET of FIB-milled cells, into three categories based on inner membrane morphology: Lamellar, approximately parallel cristae (N=10), multiple matrices (N=14), and mostly unfolded or short, tubular cristae (N=20) (Fig. 4M). It is possible that more mitochondria in our data set corresponded to the category with multiple matrices. The tomographic volumes are too thin to contain mitochondria in full and, therefore, we might not see all matrices. While we observed the smallest rupture sizes of approximately 100 nm in all three categories, increasingly larger ruptures were found for mitochondria with multiple matrices and with unfolded cristae, respectively (Fig. 4M, **p=0.0024). These results indicate that rupture size and the degree of inner membrane reshaping correlate with each other.

The mitochondria in the last category, which shared a similar degree of unfolded cristae and largely flattened inner membrane, appeared spherical (Fig. 2G, H, K, L and Fig. 4A-L). We could thus estimate the total surface area of these mitochondria, and the outer membrane area that was missing due to the rupture. The percentage of surface area that was missing varied between 2% and 50% (mean total surface area 1.15 μm^2, SD 0.41 μm^2, N=19; mean missing surface are 0.21 μm^2, SD 0.19 μm^2, N=19), and there was no correlation between size of missing surface area and total size of the mitochondrion (Fig. 4N). Thus, rupture sizes varied largely at a given stage of inner

membrane remodeling. These results indicate that, although correlated, rupture size is not solely determined by the extent of inner membrane reshaping.

The matrices of apoptotic mitochondria are dilute compared to non-apoptotic mitochondria

As cryo-ET relies on the inherent contrast of native macromolecules, differences in density within individual tomograms can be interpreted as differences in density of macromolecules. The mitochondrial matrix is a compartment of high protein concentration (Kühlbrandt, 2015). Therefore, mitochondrial matrices are expected to display a higher density in cryo-ET than the surrounding cytoplasm. However, in our data set the mitochondria with unfolded inner membranes did not appear different in density than the surrounding cytosol (Fig. 5A). To assess this observation quantitatively, we measured the ratio of average matrix-gray value to cytosol-gray value in electron cryo-tomograms of HeLa cells overexpressing GFP-Bax (Fig. 5A) (N=4 mitochondria). For comparison, we acquired electron cryo-tomograms of mitochondria in control HeLa cells that did not overexpress Bax and performed the same measurement (Fig. 5B) (N=5 mitochondria). The ratio was close to one in the cells overexpressing GFP-Bax, suggesting that the matrices of these mitochondria were similar in macromolecular density to the cytosol (Fig. 5C). In mitochondria of control cells, the ratio was significantly lower (Fig. 5C, ****$p<0.0001$), as expected for a compartment higher in macromolecular density than the cytosol. These results indicate that the mitochondria

that had unfolded inner membranes in Bax-overexpressing cells had dilute matrices as compared to control cells.

The organization of ATP synthases in apoptotic mitochondria exhibits localized changes

The dilute matrices allowed us to see individual protein complexes within the mitochondria of Bax-overexpressing HeLa cells, usually obscured by the high protein density (Kühlbrandt, 2015). In particular, ATP synthase heads were recognizable. As studied by cryo-ET of purified mitochondria, ATP synthases are localized at the ridges of cristae, where their distinct dimerization is thought to contribute to cristae structure (Anselmi et al., 2018; Davies et al., 2012; Strauss et al., 2008). We investigated the distribution of ATP synthases in apoptotic mitochondria (Fig. 5F-H; *arrowheads*). ATP synthases were abundant on cristae (Fig. 5F and F'; *matching arrowheads*). Albeit more rarely, ATP synthases were also present on shallow indentations of the boundary membrane, the region of the inner membrane directly opposed to the outer membrane (Fig. 5G and G'). No ATP synthase heads were observed on the smooth regions of the inner membrane exposed to the cytosol by the ruptured outer membrane (Fig. 5H and H'). Thus, the frequency of observing ATP synthases appeared to correlate with membrane curvature and the localization seemed to require an intact, adjacent outer membrane.

We next investigated the dimeric states of the ATP synthases on cristae and boundary membranes. The ATP synthase dimer is reported to comprise an angle of 70 -

287 100˚ between the major stalks (Davies et al., 2011; Hahn et al., 2016). On cristae,
288 dimers were readily discernable (Fig. 5F). Within these dimers, we measured the angle
289 enclosed by the two heads and the membrane between the two monomers (Fig. 5I).
290 The average angle was 106˚ (SD 18˚, N=85 dimers). Note that 106˚ measured in this
291 way correspond to approximately 70˚ between the major stalks. On the boundary
292 membrane it was not possible to unambiguously identify dimers among ATP synthases
293 (Fig. 5G). We therefore measured all possible angles between neighboring ATP
294 synthases (Fig. 5J). These measurements thus included potential dimers as well as
295 monomers positioned near to each other. For 52 ATP synthases on boundary
296 membranes, we measured 66 angles between ATP synthase pairs (Fig. 5J). The
297 average angle was 53˚ (SD 15˚), and only three ATP synthase pairs enclosed angles
298 within the range we had measured for dimers in cristae, indicating that the majority of
299 ATP synthases on the boundary membrane were not arranged into dimers similar to
300 those on cristae. These results suggest that Bax-mediated flattening of the inner
301 membrane is coupled to changes in the supramolecular organization of ATP synthases.
302 These changes involve the dissociation of dimers into monomers upon unfolding of
303 cristae, and clearance of ATP synthase heads from areas of smooth, cytosol-exposed
304 inner membrane segments.
305
306 **Bax activity can result in mitochondrial matrices entirely devoid of outer**
307 **membrane**

Recently, leakage of mtDNA into the cytosol of apoptotic cells was reported as a result of expulsion of inner membrane compartments through ruptured outer membranes (McArthur et al., 2018). In our correlative microscopy data from resin-embedded apoptotic Bax/Bak DKO HCT116 cells stably expressing GFP-Bax, MitoTracker signals localized to clumps of electron-dense compartments that were adjacent to GFP-Bax spots (Fig. 6A-D). In cryo-ET data of these cells prepared by FIB-milling, we also found compartments that contained granular structures similar to those in the mitochondrial matrix (Fig. 6E and Wolf et al., 2017), and highly curved membranes lined with particles reminiscent of ATP synthases (Fig. 6E-I). To determine whether these compartments consisted of inner mitochondrial membranes, we tested whether the particles corresponded to ATP synthases by comparing them to the ATP synthases we identified in HeLa cells (Fig. 5). We therefore measured the shortest distance from the center of the head to the membrane. The average distance was similar in both data sets (Fig. 6J; HCT116: 12.01 nm, SD 17.1 nm, N=65; HeLa: 12.07 nm, SD 1.00 nm, N=65), and matched estimates from known ATP synthase structures (Hahn et al., 2016; Hahn et al., 2018; Srivastava et al., 2018). We concluded that these particles were ATP synthases, and therefore these compartments corresponded to mitochondrial inner membranes lacking an outer membrane. These results indicate that Bax activity can result in complete removal of the outer membrane.

DISCUSSION

Three major ultrastructural processes have been associated with Bax/Bak activity and thus with the release of apoptotic factors from the intermembrane space of mitochondria during apoptosis. One is the necessity of Bax/Bak to associate into large oligomeric assemblies in the cytosol known as clusters, which follows insertion of activated Bax/Bak in the outer mitochondrial membrane (Grosse et al., 2016; Nechushtan et al., 2001; Uren et al., 2017; Zhou and Chang, 2008). The second is the occurrence of large “macropores” in the outer mitochondrial membrane, presumably for egress of apoptotic factors as well as mtDNA (Grosse et al., 2016; McArthur et al., 2018; Riley et al., 2018; Salvador-Gallego et al., 2016). The third is remodeling of the inner membrane, suggested to ensure complete release of the cytochrome *c* pool that resides predominantly in cristae (Ban-Ishihara et al., 2013; Frezza et al., 2006; Scorrano et al., 2002). There is however no unifying model on how these three major events are coupled to each other, to what extent each of them contributes to the release of apoptotic factors, and how Bax/Bak mediates all these events.

Here, we analyzed at high resolution the structural changes occurring at, and in, mitochondria of cultured human cells upon apoptotic Bax activity. We found that Bax clusters localized adjacent to ruptures of the outer membrane. We observed a single occurrence of the inner membrane being ruptured as well. Release of mtDNA has been recently associated with Bax/Bak activity and shown to involve inner membrane permeabilization (McArthur et al., 2018; Riley et al., 2018). Our observation provides

visual evidence that Bax activity can rupture the inner membrane similarly to the outer membrane, albeit in our experimental setup this was a very rare event.

In HeLa cells apoptotic due to Bax overexpression, outer membrane ruptures varied between 30 and 700 nm in diameter, consistent with the sizes of Bax-rings and arcs reported by super-resolution FM (Grosse et al., 2016; Salvador-Gallego et al., 2016). This wide range of sizes could represent either different stages of progressive rupture widening, or inherent diversity at end stages of rupture formation. During drug-induced apoptosis in HCT116 cells, we also observed mitochondrial inner membrane compartments free from an encapsulating outer membrane, reminiscent of the recently reported, herniated inner membranes attributed a role in mtDNA signaling (McArthur et al., 2018; Riley et al., 2018). In HeLa cells, the mitochondrial surface area exposed by the rupture was highly variable but did not exceed 50%. The naked inner membranes we observed in HCT116 cells thus suggest that, in addition to inherent variability of rupture sizes, the degree of outer membrane removal varies even more among cell types and/or means of apoptosis induction.

Our data depicts ultrastructural and molecular details of the inner membrane architecture upon Bax activity. We observed fragmentation of the inner membrane compartments without outer membrane fission. We found that cristae locally unfolded into short, tubular protrusions and shallow ridges, accompanied by disassembly of ATP synthases from dimers into loosely associated monomers. Furthermore, inner membrane segments exposed to the cytosol by outer membrane ruptures appeared very smooth, displayed a consistently low curvature, and were completely devoid of

ATP synthase heads. This shows that cristae unfolding and ATP synthase disintegration are maximal at outer membrane ruptures. We also observed a decreased density of macromolecules in the matrix of these mitochondria, indicating dilution of the matrix content. This observation implies swelling and dilation of the inner membrane compartment, likely to generate turgor pressure and high membrane tension, which could facilitate cristae unfolding and disruption of the ATP synthase organization. The angular arrangement of ATP synthase dimers in cristae of Bax-affected mitochondria was similar to what has been reported for other species (Davies et al., 2011; Hahn et al., 2016), though our data presented a large range of dimer angles (Fig. 5J). This range could be either due to inherent variability of ATP synthase dimers in human cells, or could reflect initial stages of dimer disassembly. It is thought that ATP synthase dimers induce membrane curvature, thereby contributing to the shape of cristae and to the proton-motive force (Anselmi et al., 2018; Davies et al., 2012; Hahn et al., 2016; Strauss et al., 2008). Disassembly of ATP synthase organization has been associated with loss of mitochondrial function and with aging (Daum et al., 2013). Here we show that a local, distinctive two-stage disassembly of ATP synthases is part of Bax-mediated loss of cristae structure implicated in the release of apoptotic factors. This is particularly relevant as the loss of membrane curvature could help setting cytochrome *c* free, which is bound to cardiolipin in the intracristal space (Scorrano et al., 2002; Speck et al., 1983; Vik et al., 1981).

It is also worth noting that the smooth inner membrane exposed to the cytosol is remarkably similar to cryo-ET images from mouse embryonic fibroblasts shown by

McArthur et al. (2018). This corroborates that the localized changes to the inner membrane we report here are general principles of Bax-mediated apoptosis.

Our quantitative analysis shows that the largest ruptures are found on mitochondria with almost completely unfolded cristae. This suggests a mechanism by which the inner membrane rearrangements could contribute to rupture formation: As the inner membrane flattens, the mismatch between inner and outer membrane surface area exerts pressure onto the outer membrane. This pressure could cause rupturing of outer membrane areas that are locally destabilized, for instance through accumulation of membrane-inserted Bax (Westphal et al., 2014). Further inner membrane flattening could widen initial ruptures. This mechanism could in principle generate large ruptures without removal of lipids from the outer membrane.

We also observed that rupture sizes vary largely even at a given stage of inner membrane reorganization, indicating that additional factors impact on rupture size and thus are potential contributors to rupture formation. One possible factor could be the amount of membrane-inserted, accumulated Bax molecules generating tension in the outer membrane (Westphal et al., 2014).

The details we reveal on the ultrastructure of Bax clusters suggest that clusters might also be contributing to rupture formation. We found that Bax clusters have a higher-order organization consisting of interconnected planes or discs arranged in an irregular manner, reminiscent of a sponge-like meshwork. The lipid bilayer edges of the ruptures often appeared embedded in this meshwork or connected to its structural features. Some of the sharp edges within the meshwork resemble side views of

membranes, suggesting that the clusters might contain patches of membrane. Previous models proposed that Bax/Bak cluster activity involves generating membrane tension, which is released by remodeling the bilayer of the planar outer membrane into a non-lamellar lipid arrangement (Nasu et al., 2016; Uren et al., 2017). This remodeling could be aided by membrane sculpting proteins such as N-BAR domain proteins (Gallop et al., 2006). The N-BAR protein endophilin B1 interacts with Bax during apoptosis in cultured cells (Takahashi et al., 2005) and, also through interaction with Bax, causes vesiculation of liposomes *in vitro* (Etxebarria et al., 2009; Rostovtseva et al., 2009). Notably, the related N-BAR protein endophilin A1 can generate interconnected tubular membrane networks (Ayton et al., 2009; Simunovic et al., 2013). Furthermore, lipids such as cardiolipin and ceramides were attributed roles in supporting Bax activity (Jain et al., 2017; Kuwana et al., 2002). Thus, we speculate that the higher-order meshwork we observe for Bax clusters is a result of Bax reshaping outer membrane patches from a lamellar topology into a non-lamellar bilayer network, similar to sponge-like lipid cubic phases (Valldeperas et al., 2016). This model would suggest that ruptures might be formed through removal of lipids from the outer membrane. It would additionally explain how the clusters form: Bax oligomerization requires the interaction with membranes (Bleicken et al., 2010), while clusters occupy a volume in the cytosol. Therefore, there must be a transition from accumulation of Bax molecules in the membrane plane to a three-dimensional cluster of Bax molecules. Following association within the outer membrane, Bax might progressively deform the membrane into a meshwork-like structure, which grows as more Bax molecules accumulate and serves as a sink for

437 outer membrane components (Uren et al., 2017). Thus, the formation of the wide range
438 of rupture sizes observed by others and us might be a consequence of two
439 mechanisms: Cristae unfolding leading to flattening of the inner membrane, and
440 sequestration of outer membrane components into Bax clusters.

441 In summary, we reveal molecular and morphological details of the effects of Bax
442 activity on inner and outer mitochondrial membranes, suggesting how they collectively
443 contribute to the release of apoptotic factors from mitochondria. Our study provides a
444 comprehensive model on how reorganizations of the supramolecular architecture of
445 membranes interplay to drive apoptosis.
446

ACKNOWLEDGEMENTS

We thank Julia Mahamid for instruction and advice on cryo-FIB milling, Christos Savva, Giuseppe Cannone and Shaoxia Chen for EM support, Christopher Russo for advice and help with the Scios microscope. Work in the group of W.K. is supported by the Medical Research Council (MC_UP_1201/8). Work in the group of R.J.Y. is supported by the NIH National Institute of Neurological Disorders and Stroke Intramural Research Program. N.R.A. was supported by a Marshall Scholarship and the NIH-Oxford-Cambridge Scholars Program.

MATERIALS AND METHODS

Cell culture: HeLa cells for all Bax experiments were grown at 37˚C, 5% CO_2 in DMEM, high glucose, GlutaMAX, pyruvate (Thermo 31996) medium supplemented with 10% heat-inactivated FBS (Gibco 10270), 10 mM HEPES, and 1× NEAA (Thermo 11140). Control HeLa cells for matrix density measurements were grown at 37˚C, 5% CO_2 in DMEM, high glucose, GlutaMAX, pyruvate (Thermo 31996) medium supplemented with 10% heat-inactivated, Tet-approved FBS, (Pan Biotech p30-3602), 0.2 µg/mL hygromycin B (Invitrogen 10687010), 10 mM HEPES, and 1× NEAA (Thermo 11140). Bax/Bak DKO HCT116 GFP-Bax cells were grown at 37˚C, 5% CO_2 in McCoy's 5A, GlutaMAX medium (Thermo 36600) supplemented with 10% heat-inactivated FBS (Gibco 10270), 10 mM HEPES, and 1× NEAA (Thermo 11140).

468 **Constructs and reagents:** hBax-C3-EGFP (Addgene plasmid 19741)
469 (Nechushtan et al., 1999) was used for transient GFP-Bax expression in HeLa cells.
470 Transient transfection was performed using X-tremeGENE 9 (Roche 06365787001) at a
471 ratio of 3 µL of transfection reagent to 1 µg DNA. MitoTracker Deep Red (Thermo
472 22426) was used for cellular staining at 20 nM. Drug treatments used were ABT-737 at
473 10 µm (Cayman 11501) and Q-VD-OPh at 10 µM (APExBIO, A1901).
474
475 **Live-cell confocal microscopy:** HeLa cells were grown in 2-well chamber slides
476 (iBidi 80286), stained with MitoTracker Deep Red, transfected with 1000 ng hBax-C3-
477 EGFP plasmid and incubated with Q-VD-OPh. Bax/Bak DKO HCT116 GFP-Bax cells
478 were grown in 2-well chamber slides, stained with MitoTracker Deep Red, and
479 incubated with ABT-737 and Q-VD-OPh. Both cell lines were imaged every 30 min.
480 Imaging was performed with a Zeiss LSM 710 confocal microscope with a 63× Plan Apo
481 oil-immersion objective with NA=1.4. GFP-Bax and MitoTracker Deep Red were excited
482 at 488 and 647 nm, respectively. For both cell lines, the live-imaging experiments were
483 repeated at least three times.
484
485 **Immunofluorescence microscopy:** HeLa cells were plated onto 13 mm cover
486 glasses (Assistant, 41001113) in a 24-well plate, transfected with 300 ng hBax-C3-
487 EGFP plasmid and incubated with Q-VD-OPh for 16 h. Cells were then fixed with 4%
488 paraformaldehyde in phosphate buffer saline (PBS), pH 7.2 for 30 min. The cover
489 glasses containing cells were removed from the plate, blocked for 1 h in 10% goat

serum (Sigma G6767) and 1% Saponin (Sigma 8047-15-2) and incubated overnight at 4°C with 1:250 mouse anti-cytochrome *c* antibody (BD Pharmingen 556432) and 1:250 rabbit polyclonal anti-TOM20 antibody (Santa Cruz Biotechnology; sc-11415). The samples were then incubated with 1:200 Alexa-Fluor anti-rabbit-405nm and Alexa-Fluor donkey anti-mouse-647nm antibodies (Invitrogen; A31556 and A31571) for 1 h at room temperature and mounted with ProLong Diamond Antifade Mountant (Invitrogen) on an imaging slide. Imaging was performed on a Zeiss LSM 710 confocal microscope with a 63× Plan Apo oil-immersion objective with NA=1.4.

Correlative FM and ET of resin-embedded cells: Correlative microscopy of resin-embedded cells was performed as described in (Ader and Kukulski, 2017). In brief, cells were grown on 3 mm sapphire disks (Engineering Office M. Wohlwend, Switzerland) in 6-well plates for 24 h, transfected with 2000 ng hBax-C3-EGFP plasmid and incubated with Q-VD-OPh for 16 h, stained with MitoTracker Deep Red, and high-pressure frozen using a HPM100 (Leica Microsystems), screened for quality of cell distribution and for GFP-Bax expression by cryo-FM (Leica EM Cryo CLEM, Leica Microsystems) equipped with an Orca Flash 4.0 V2 sCMOS camera (Hamamatsu Photonics) and a HCX PL APO 50× cryo-objective with NA = 0.9. For screening, a 2 × 2 mm montage was taken of green (L5 filter, 250 ms), far red (Y5 filter, 100 ms), and brightfield (50 ms) channels (all filters: Leica Microsystems). Z-stacks were collected regions of interest (0.5 µm intervals) over a region of interest 0.6 x 0.6 mm with the same exposure settings. Cells were then freeze-substituted with 0.008% uranyl acetate

512 in acetone and embedded in Lowicryl HM20 using a AFS2 (Leica Microsystems). Resin-
513 embedded cells were then sectioned 300 nm thin using a Ultracut E Microtome
514 (Reichert) and a diamond knife (Diatome), and collected on 200 mesh copper grids with
515 carbon support (S160, Agar Scientific Ltd.). As fiducial markers for correlation, 50 nm
516 TetraSpeck microspheres (custom order, Invitrogen) diluted 1:100 in PBS pH 8.4 were
517 adsorbed for 5-10 min to the sections. Fluorescence images were acquired using a
518 TE2000-E widefield fluorescence microscope (Nikon) with a 100× oil-immersion TIRF
519 objective with NA=1.49. Filters: 89006 ET CFP/YFP/mCherry (Chroma), excitation
520 560/20, dichroic 89008bs, emission 535/30 for YFP-Parkin and 49006 ET CY5
521 (Chroma), excitation 520/60, dichroic T660lpxr, emission 700/75 for MitoTracker Deep
522 Red. Fiducial markers were visible in both channels. Transmission EM (TEM) images at
523 approximately 100 µm defocus were collected using the montaging function in SerialEM
524 (Mastronarde, 2005) at a region of interest, at a pixel size of 1.1 nm. Correlation
525 between fluorescence images and TEM montaged images was performed using the
526 fiducial marker positions as previously described (Ader and Kukulski, 2017; Kukulski et
527 al., 2011). ET was done on a Technai F20 (FEI) operated at 200 kV in STEM mode on
528 an axial bright field detector. Tilt series were collected using a high-tilt tomography
529 holder (Fischione Instruments; Model 2020) from approximately -65˚ to +65˚ (1˚
530 increments) at a pixel size of 1.1, 1.6, 2.9, 3.1, or 4.4 nm. Reconstruction and
531 segmentation were performed using IMOD (Kremer et al., 1996). The data set on resin-
532 embedded HeLa cells has been acquired from cells grown on two different sapphire
533 disks, vitrified during the same high-pressure freezing session. The data set on resin-

534 embedded Bax/Bak DKO HCT116 has been acquired from cells grown on one sapphire
535 disk. See also Suppl. Table T1. Segmentations and figures were made from tomograms
536 acquired at 1.1 nm pixel size. For better visibility in all figures, we used tomograms
537 filtered with nonlinear anisotropic diffusion (NAD) and reduced noise in the virtual slices
538 shown by using a Gaussian filter in IMOD.
539
540 **Cryo-FIB milling:** HeLa cells were grown for 24 h on 200 mesh gold grids with a
541 holey carbon film R2/2 (Quantifoil) in 6-well plates and transfected with 2000 ng hBax-
542 C3-EGFP plasmid in presence of Q-VD-OPh. 16 hours after transfection, cells were
543 stained with MitoTracker Deep Red, grids were manually backside blotted using
544 Whatman filter paper No. 1 and vitrified using a manual plunger. Bax/Bak DKO HCT116
545 GFP-Bax cells were grown on grids for 36 h, stained with MitoTracker Deep Red, and
546 incubated with ABT-737 and Q-VD-OPh for 3 h before plunge-freezing. Control HeLa
547 cell for measurements of matrix density contained a doxycycline-inducible Fsp27-EGFP
548 construct and were prepared for an unrelated project by treating with 0.4 mM oleic acid
549 (Sigma, O3008) and 1 µg/mL doxycycline (Takara, 631311) for 15 h before incubation
550 with 1× LipidTox Deep Red (Thermo, H34477) for 1 h, and then plunge-frozen as
551 described above. Grids were screened for cells with GFP-Bax expression using by cryo-
552 FM (Leica EM Cryo CLEM, Leica Microsystems), equipped with an Orca Flash 4.0 V2
553 sCMOS camera (Hamamatsu Photonics) and a HCX PL APO 50× cryo-objective with
554 NA = 0.9, in a humidity-controlled room (humidity below 25%). For screening, a 1.5 ×
555 1.5 mm montage was taken of green (L5 filter, 250 ms), far red (Y5 filter, 100 ms), and

brightfield (50 ms) channels (all filters: Leica Microsystems). Z-stacks were collected of grid squares of interest (0.5 µm intervals) over the cell volume with the same exposure settings. Cells were cryo-FIB milled to prepare lamellae using a Scios DualBeam FIB/SEM (FEI) equipped with a Quorum cryo-stage (PP3010T), following the protocol described in Schaffer et al. (2015). In brief, grids were coated with an organic Pt compound using the gas injection system for either 8 s at 12 mm working distance or 30 s at 13 mm working distance from a stage tilt of 25˚. The stage was then tilted so that the grid was at a 10˚ angle towards the ion beam for all subsequent steps. The electron beam was used at 13 pA and 5-10 kV to locate cells, 2 kV for subsequent imaging. The ion beam was used at 30 kV and 10 pA for imaging. Rough milling was performed at 30 kV ion beam voltage, and subsequently the current was reduced from 0.5 nA to 0.1 nA until a lamella thickness of 5 µm was reached, and further to 0.1 nA until 1 µm lamella thickness. Fine milling to a final lamella thickness of approximately 200 nm was performed at 16 kV and 11 pA ion beam setting.

Vitreous sectioning and correlative microscopy of vitreous sections: HeLa cells were grown for 24 h in 6-well plates, transfected with 2000 ng hBax-C3-EGFP plasmid and incubated with Q-VD-OPh for 16 h, then trypsinized and pelleted. Immediately before trypsinizing, cells were stained with MitoTracker Deep Red. Pellets were maintained at 37˚ C while they were mixed 1:1 with 40% Dextran (Sigma) in PBS, pipetted into the 0.2 mm recess of gold-coated copper carriers, covered with the flat side of Aluminum carriers B and high-pressure frozen with a Leica HPM100 (Leica

578 Microsystems). 100 nm thick vitreous sections were produced at -150˚ C in a UC6/FC6
579 cryo-ultramicrotome (Leica Microsystems) using cryotrim 25 and a 35˚ cryo immuno
580 knives (Diatome). The sections were attached using a Crion antistatic device (Leica
581 Microsystems) to EM grids (R3.5/1, copper, Quantifoil) that were plasma cleaned and
582 had 100 nm TetraSpeck beads (Invitrogen) diluted 1:50 in PBS adhered to them. To
583 identify areas in the sections that contained GFP-Bax signals and were suitable for
584 cryo-ET, we used the procedure described in (Bharat et al., 2018). In brief, grids with
585 vitreous sections were imaged by cryo-FM on the Leica EM Cryo CLEM (Leica
586 Microsystems), equipped with an Orca Flash 4.0 V2 sCMOS camera (Hamamatsu
587 Photonics) and a HCX PL APO 50× cryo-objective with NA = 0.9, in a humidity-
588 controlled room (humidity below 25%). For screening, a 1.5 × 1.5 mm montage was
589 taken of green (L5 filter, 1 s), far red (Y5 filter, 1 s), and brightfield (50 ms) channels (all
590 filters: Leica Microsystems). TetraSpecks were visible in both green and far red. Z-
591 stacks were collected of grid squares of interest (0.3 µm intervals) over the section
592 volume of green (L5 filter, 3 s), far red (Y5 filter, 3 s), and brightfield (50 ms) channels.
593 Localization of GFP signals in cryo-EM intermediate magnification maps was done by
594 visual correlation, as described in (Bharat et al., 2018). Subsequent precise correlation
595 was done using custom MATLAB-based scripts (Kukulski et al., 2012; Schorb and
596 Briggs, 2014). However, because in many areas of the grids, TetraSpeck fiducial
597 markers were sparse, we instead used the centers of carbon film holes as landmarks for
598 correlation between cryo-FM and cryo-EM images.
599

Electron cryo-tomography of cryo-FIB milled lamellae and vitreous sections: Montaged images of the entire grid were acquired at low magnification at pixel size of 182.3 nm for vitreous sections and either 190.9 or 99.4 nm for lamella. Intermediate magnification maps of grid squares with vitreous sections or lamella of interest were acquired at pixel size 5.5 nm. Electron cryo-tomographic tilt-series were collected on a Titan Krios (FEI) operated at 300 kV using a Quantum energy filter (slit width 20 eV) and a K2 direct electron detector (Gatan) in counting mode at a pixel size of 3.7 Å and at a dose rate of ~ 2-4 e^-/pixel/second on the detector, dependent on sample thickness. Tilt-series were acquired between ±60° starting from 0° with 1° increment using SerialEM (Mastronarde, 2005) following a grouped dose-symmetric acquisition with a group size of 4 (Bharat et al., 2018; Hagen et al., 2017), and at -5 µm defocus. A dose of approximately 1.0 to 1.2 $e^-/Å^2$ was applied per image of the tilt-series. Reconstruction and segmentation were performed using IMOD (Kremer et al., 1996). The vitreous sections data has been acquired on sections produced from one high-pressure frozen pellet of one HeLa cell culture. The HeLa (GFP-Bax overexpression) lamellae data has been acquired on 5 different lamellae (each lamellae corresponding to one cell) produced from 3 separate plunge-freezing sessions, thus 3 separate cell culture experiments. The HeLa control lamellae data has been acquired on 2 lamellae from 2 separate plunge-freezing sessions. The Bax/Bak DKO HCT116 lamellae data has been acquired on one lamella corresponding to one cell. See also Suppl. Table T1.

Segmentations shown in Fig. 3M and P only represent those parts of the membranes that were well visible in the electron cryo-tomograms. Due to the anisotropic resolution of electron tomograms, membranes that are oriented at shallow angles or parallel relative to the section plane are difficult to see. We therefore did not segment regions of mitochondria in which we could not unambiguously determine membrane position or connectivity. Ends of the segmentation are indicated in white in Fig. 3M. For better visibility in all figures, we used tomograms reconstructed by simultaneous iterative reconstruction technique (SIRT) (10 iterations), binned to a pixel size of 7.5 Å, and reduced noise in the virtual slices shown by using both a 3D Median and a Gaussian filter in IMOD. For movies, the tomographic volumes were filtered as a whole in IMOD.

Quantifications and Statistical Analysis: We estimated the size of outer membrane ruptures (Fig. 4M) by measuring the shortest distance between the two edges visible in a single virtual slice of the electron tomogram using IMOD. In some cases, parts of the membrane were oriented at oblique angles relative to the tomographic image plane. Due to the anisotropic resolution of electron tomograms, these membrane parts were difficult to discern and therefore rupture sizes could not be estimated. Rupture size distributions of the three inner membrane morphologies were compared using an ordinary one-way ANOVA with Tukey's multiple comparisons test, assuming that the datasets are normally distributed (significance shown in Fig. 4M). The mitochondria diameters used to calculate total surface area were estimated by

643 measuring the furthest distance between outer membranes in a single virtual slice of the
644 electron tomogram using IMOD. Surface area of the whole mitochondrion was
645 calculated with the formula for surface area of a sphere, while surface area of the
646 missing segment was calculated with the formula for surface area of a spherical cap
647 (Fig. 4N).

648 For estimations of mitochondrial matrix density, we used cryo-ET data of cryo-
649 FIB milled, non-apoptotic HeLa cells acquired as a side product in the context of an
650 unrelated project, which here served as the control. Density ratios were quantified as
651 the ratio of average gray values taken from twelve randomly selected areas of 30 nm
652 radius within the matrix, to the grey values of twelve randomly selected areas of the
653 same size taken in the cytosol within the same virtual tomographic slice using ImageJ
654 (Fig. 5C). We calculated this ratio for 4 virtual slices from each of 4 different electron
655 tomograms each from Bax-overexpressing and control Hela cells. These values were
656 compared using a two-tailed, unpaired t test with Welch's correction, assuming that the
657 datasets are distributed normally (significance is shown in Fig. 5C).

658 To measure the angle between ATP synthase heads, contours of 3 points were
659 made in IMOD at the center of the heads of two neighboring ATP synthases and in the
660 middle of the inner membrane between the two heads. The distance between all three
661 points was measured, and the law of cosines was used to calculate the angle between
662 heads.

663 To identify ATP synthases in compartments without outer membrane in HCT116
664 cells, we used IMOD to measure the distances between putative ATP synthase head

665 and inner membrane in either an intact mitochondrion or the unknown compartment
666 (Fig. 6J). These values were compared using a two-tailed, unpaired t-test with Welch's
667 correction, assuming that the datasets are distributed normally (significance is shown in
668 Fig. 6J).
669

FIGURE LEGENDS

Figure 1. Live confocal fluorescence microscopy of HeLa cells overexpressing GFP-Bax. HeLa cells transfected with GFP-Bax (green) in the presence of Q-VD-OPh were imaged every 30 min, for 24 h after transfection. Cells were stained with MitoTracker Deep Red (magenta) prior to imaging. **A:** Representative cell 9 h after transfection. **B:** Representative cell 14 h after transfection, showing formation of GFP-Bax punctae. **C:** Larger clusters of GFP-Bax in a representative cell 19 h after transfection. White boxes indicate areas shown magnified below the large image. The three magnified images correspond to: GFP-Bax channel (left), MitoTracker Deep Red channel (middle), and merge (right). Scale bars: 5 μm (upper panel) and 2 μm (lower panel).

Figure 2: Correlative microscopy of resin-embedded HeLa cells overexpressing GFP-Bax. Gallery of GFP-Bax locations and the associated mitochondrial morphologies, 16 h post-transfection with GFP-Bax, in the presence of Q-VD-OPh. **A-D:** FM images of sections of resin-embedded cells. GFP-Bax (green) and MitoTracker Deep Red (magenta). White squares indicate the field of view imaged by ET. White crosses indicate centroids of GFP-Bax signals localized in electron tomograms. **E-H:** Virtual slices from electron tomograms acquired at areas indicated by white squares in A-D, respectively. Red circles mark representative ribosomes in intermembrane space. White arrowheads indicate membrane ruptures. Green crosses indicate predicted positions of GFP-Bax signals corresponding to white crosses in fluorescence

692 micrographs. **I-L:** 3D segmentation model of mitochondria in E-H, respectively. Outer
693 membranes are in dark blue, inner membranes in light blue and ribosomes in the
694 intermembrane space in white. Scale bars: 1 µm (A-D), 100 nm (E-L).
695
696 **Figure 3. Ultrastructure of GFP-Bax clusters in HeLa cells visualized by cryo**
697 **correlative microscopy of vitreous sections, and by cryo-ET of FIB-milled cells. A,**
698 **E**: Cryo-FM of vitreous sections of HeLa cells (high-pressure frozen 16 h post-
699 transfection with GFP-Bax). GFP-Bax signal in green. White squares indicate areas
700 shown in B and F, respectively. **B, F:** Cryo-EM overview images of areas shown in
701 white squares in A and E, respectively. The corresponding cryo-FM images,
702 transformed according to correlation procedure, are overlaid in green. White dashed
703 squares indicate areas imaged by cryo-ET. **C, G:** Virtual slices through electron cryo-
704 tomograms corresponding to white dashed squares in B and F, respectively. Black
705 squares indicate areas magnified in D, H, respectively. **D, H:** Magnifications of virtual
706 slices shown in C and G, respectively, areas corresponding to black squares. **D', H'**:
707 Annotation of images in D and H, respectively. Structural features of the GFP-Bax
708 cluster ultrastructure are highlighted in red. **I, L, O:** Virtual slices through electron cryo-
709 tomograms of HeLa cells (plunge-frozen 16 h post transfection with GFP-Bax), targeted
710 by cryo-FM (see Suppl. Fig. S3) and thinned by cryo-FIB milling. Note that L and O
711 show different virtual slices of the same mitochondrion; rotated by 180° around the
712 image y-axis. Black squares indicate areas magnified in K, N and Q, respectively.
713 Yellow and red arrowheads indicate ruptured outer and inner membranes, respectively.

714 **J, M and P:** 3D segmentation model of mitochondria seen in I, L and O, respectively.
715 Outer membranes are in dark blue, inner membranes in light blue, and ribosomes in
716 intermembrane space in white (J). White borders (M) indicate end of segmentation (see
717 Materials and Methods). Note that M and P show the same mitochondrion at different
718 viewing angles and magnifications. **K, N and Q:** Magnifications of virtual slices shown in
719 I and L, respectively, areas corresponding to the black squares. Yellow and red
720 arrowheads indicate ruptured outer and inner membranes, respectively. **K', N' and Q'**:
721 Annotation of images in K, N and Q, respectively. Structural features of the cluster
722 ultrastructure are highlighted in red. Scale bars: 1 µm (A, E), 500 nm (B, F), 100 nm (C,
723 G, I, J, L, M, O, P), 50 nm (D, D' H, H' K, K', N, N', Q, Q').
724
725 **Figure 4. Mitochondrial outer membrane ruptures are accompanied by**
726 **rearrangements of the inner membrane. A-C:** Virtual slices through electron cryo-
727 tomograms of HeLa cells (16 h post transfection with GFP-Bax), thinned by cryo-FIB
728 milling. Black squares indicate areas magnified in D-I, respectively. **D-I:** Magnifications
729 of the virtual slices shown in A-C, respectively, areas corresponding to black squares.
730 White arrowheads indicate ruptured membranes. **J-L:** 3D segmentation model of
731 mitochondria seen in A-C, respectively. Outer membranes are in dark blue, inner
732 membranes in light blue. **M:** Quantification of rupture sizes, grouped according to inner
733 membrane morphology category. Data points are from both ET of resin-embedded
734 HeLa cells, and from cryo-ET of cryo-FIB milled HeLa cells, all 16 h post-transfection
735 with GFP-Bax. Schematic representation of each category is shown above columns.

736 **p=0.0024 for lamellar cristae vs. unfolded cristae. The red lines indicate the mean and
737 the standard deviation. **N:** Surface area of the missing outer membrane segment plotted
738 against the surface area of the total mitochondrial outer membrane, for mitochondria
739 with mostly flattened inner membranes (indicated by schematic in upper right corner).
740 Scale bars: 100 nm (A-C and J-L), 20 nm (D-I).
741
742 **Figure 5. Dilution of the mitochondrial matrix and organization of ATP synthases**
743 **visualized by cryo-ET of cryo-FIB milled HeLa cells. A:** Virtual slice through an
744 electron cryo-tomogram of a HeLa cell (16 h post-transfection with GFP-Bax) thinned by
745 cryo-FIB milling. **B**: Virtual slice through an electron cryo-tomogram of a control HeLa
746 cell thinned by cryo-FIB milling, showing typical mitochondria in absence of GFP-Bax
747 expression. **C:** Quantitative analysis of the ratio between average gray values in the
748 matrix and average gray values in the cytosol. ****p<0.0001 for comparison between
749 mitochondria in GFP-Bax overexpressing and control HeLa cells. The red lines indicate
750 the mean and the standard deviation. **D:** Virtual slice through an electron cryo-
751 tomogram of a HeLa cell (16 h post-transfection with GFP-Bax), thinned by cryo-FIB
752 milling. Black squares indicate areas magnified in F-H. **E:** 3D segmentation model of
753 mitochondrion seen in D. Outer membranes are in dark blue, inner membranes in light
754 blue, and ATP synthase heads in red. **F-H:** Magnified areas of the virtual slice shown in
755 D, corresponding to the black squares. White arrowheads indicate ATP synthase heads.
756 Arrowheads of matching color in G denote dimers of ATP synthases. **F'-H':** Images
757 from F-G shown with the segmentation model from E. Outer membranes are in dark

758 blue, inner membranes in light blue, and ATP synthase heads in red. **I:** Structure of the
759 yeast ATP synthase dimer (EMD-2161, Davies et al., 2012), to illustrate how we
760 measured the angle enclosed by ATP synthases heads and membrane (yellow points
761 and dashed lines) for our analysis. **J:** ATP synthase angles measured in dimers in
762 cristae membranes, and between neighboring ATP synthases in the boundary
763 membrane (BM). The red lines indicate the mean and the standard deviation. Scale
764 bars: 100 nm (A, B, D, E), 20 nm (F, F', G, G', H, H').
765
766 **Figure 6. HCT116 cells treated with the apoptotic drug ABT-737 contain inner**
767 **membrane compartments that are lacking the enclosing outer membranes. A:** FM
768 of a section of resin-embedded Bax/Bak DKO HCT116 cells stably expressing GFP-
769 Bax, treated with ABT-737 for 3 h. GFP-Bax (green), MitoTracker Deep Red (magenta).
770 White square indicates the field of view imaged by ET, white crosses indicate
771 fluorescent signals of interest localized in electron tomograms. **B:** Virtual slice through
772 an electron tomogram acquired at area indicated by the white square in A. Green and
773 magenta crosses indicate predicted position of GFP-Bax and MitoTracker Deep Red
774 signals, respectively. Black square indicates area magnified in C. **C:** Magnified area of
775 the virtual slice shown in B, corresponding to the black square. The image shows an
776 accumulation of single membrane compartments near the GFP-Bax clusters. **D:** 3D
777 segmentation model of mitochondria and single-membrane compartments seen in B.
778 Outer membranes are in dark blue, inner membranes in light blue. **E:** Virtual slice
779 through an electron cryo-tomogram of a cryo-FIB milled Bax/Bak DKO HCT116 cells

780 stably expressing GFP-Bax treated with ABT-737 3 h. Arrows indicate compartments
781 reminiscent of mitochondrial inner membranes that appear to have no outer membrane,
782 arrowhead indicates an inner membrane within an intact mitochondrion. **F, G:** Magnified
783 areas of the virtual slice shown in E, corresponding to the black squares. White
784 arrowheads indicate putative ATP synthase heads. **H:** 3D segmentation model of
785 compartments seen in E. Membranes are in light blue, putative ATP synthase heads in
786 red. White box indicates magnified area in I. **I:** Magnified and rotated area from white
787 box in H, depicting the arrangement of putative ATP synthase heads. **J:** Measured
788 distances between head and inner membrane. Comparison between ATP synthases
789 identified in mitochondria in HeLa cells, and putative ATP synthases in the
790 compartments without outer membrane in HCT116 cells. The red lines indicate the
791 mean and the standard deviation. Scale bars: 500 nm (A), 100 nm (B-E, H), 20 nm (F,
792 G, I).
793
794 **Figure 7. Model for the interplay of inner and outer membrane reorganization**
795 **during Bax-mediated steps of apoptosis.** Bax clusters form at outer membrane
796 ruptures. Clusters display a higher-order organization of their components. Ruptures
797 allow influx of ribosomes and thus mixing of cytosolic and intermembrane content. As
798 rupture size increases, the inner membrane remodels through fragmentation and cristae
799 unfolding. Dilution of the mitochondrial matrix likely supports dilation of the inner
800 membrane compartment. Inner membrane reshaping is accompanied by disassembly of
801 ATP synthase dimers into monomers and a complete clearance of ATP synthases from

802 regions of inner membrane that are exposed to the cytosol, and that are maximally
803 flattened. The degree of outer membrane removal varies, and is maximal in HCT116
804 cells, where inner membrane compartments devoid of any outer membrane can be
805 found.
806
807 **Supplementary Figure S1. Immunofluorescence of cytochrome *c* release at**
808 **different stages of GFP-Bax recruitment to mitochondria.** Confocal FM of fixed
809 HeLa cells, 16 h post-transfection with GFP-Bax (green) in the presence of Q-VD-OPh.
810 Cells were stained with antibodies for the translocase of outer membrane 20 (TOM20)
811 (magenta) and cytochrome *c* (cyan). For better visibility, the three channels are shown
812 as two separate merges of two channels at a time. A-D are merges of GFP-Bax (green)
813 with TOM20 (magenta) signals. White boxes indicate areas shown magnified to the right
814 side of the large image. The three magnified images correspond to: GFP-Bax channel
815 (top), TOM20 channel (middle), merge (bottom). A'-D' are merges of the GFP-Bax
816 (green) and cytochrome *c* (cyan) signals. White boxes indicate areas shown magnified
817 to the right side of the large image. The three magnified images correspond to: GFP-
818 Bax channel (top), cytochrome *c* channel (middle), merge (bottom). **A, A':** Cell that does
819 not express GFP-Bax. No release of cytochrome *c* from the mitochondria. **B, B'**: Cell
820 that shows small punctae of GFP-Bax and displays partial release of cytochrome *c*. **C,**
821 **C':** Cell that shows large clusters of GFP-Bax and displays partial release of
822 cytochrome *c*. **D, D':** Cell that shows large clusters of GFP-Bax and displays full release

of cytochrome *c* from the mitochondria into the cytosol. Scale bars are 10 µm (overview images) and 2 µm (magnified views).

Supplementary Figure S2. Drug-induced GFP-Bax recruitment to mitochondria causes outer membrane ruptures and inner membrane rearrangement similar to those induced in HeLa cells upon GFP-Bax overexpression. Live confocal FM of Bax/Bak DKO HCT116 cells stably expressing GFP-Bax (green), treated with ABT-737 and Q-VD-OPh for 3 h. Cells were stained with MitoTracker Deep Red (magenta) prior to treatment. Cells were imaged every 30 min for 3 h after treatment. FM images shown are from **A:** 30 min, **B:** 1 h, and **C:** 2 h 30 min following treatment. White squares indicate areas shown magnified below A-C. The three magnified images correspond to: GFP-Bax channel (left), MitoTracker channel (middle), and merge (right). **D-F:** Correlative microscopy: FM image of section of resin-embedded Bax/Bak DKO HCT116 cells stably expressing GFP-Bax (green) that were treated with ABT-737 and Q-VD-OPh for 3 h. GFP-Bax (green), MitoTracker Deep Red (magenta). **G-I:** Virtual slices from electron tomograms acquired at areas indicated by white square in FM images. White arrowheads indicate ruptured membranes. Crosses indicate predicted positions of GFP-Bax signals. **J-L:** 3D segmentation model of mitochondria in G-I, respectively. Outer membranes in dark blue, inner membranes in light blue. Scale bars: 10 µm (A-C, upper panels), 2 µm (A-C, lower panels), 1 µm (D-F), 100 nm (G-L).

844 **Supplementary Figure S3. Cryo-FM of mammalian cells and targeted cryo-FIB**
845 **milling.** Shown are all cells that were used to acquire the cryo-ET data set presented in
846 this study. A-E and G-K are HeLa cells that were grown on EM grids and plunge-frozen
847 16 h after transfection with GFP-Bax. F and L show a Bax/Bak DKO HCT116 cell stably
848 expressing GFP-Bax, that was grown on an EM grid and plunge-frozen 3 h after
849 treatment with ABT-737. GFP-Bax (green), MitoTracker Deep Red (magenta). **A-F:**
850 Cryo-FM of cells. Cells were selected for cryo-FIB milling based on the presence of
851 GFP-Bax punctae. In A, the outlines of the resulting lamella are indicated by white
852 dashed lines. **G-L:** Cryo-EM overview images of the lamellae resulting from cryo-FIB
853 milling of the cells shown in A-F, respectively. Approximate lamella thicknesses, based
854 on reconstruction data are: 150 nm (G), 240 nm (H), 200 nm (I), 280 nm (J), 180 nm
855 (K), 280 nm (L). Scale bars: 5 µm (A-L).
856
857 **Movie 1. Electron cryo-tomogram of GFP-Bax clusters obtained by correlative**
858 **microscopy of vitreous sections, corresponding to Figure 3C-D'.** Movie through
859 virtual slices of electron cryo-tomogram. Movie pauses at the virtual slice shown in Fig.
860 3D and D' to indicate structural features highlighted in red. Scale bar: 50 nm.
861
862 **Movie 2. Electron cryo-tomogram of GFP-Bax clusters obtained by correlative**
863 **microscopy of vitreous sections, corresponding to Figure 3G-H'.** Movie through
864 virtual slices of electron cryo-tomogram. Movie pauses at the virtual slice shown in Fig.
865 3H and H' to indicate structural features highlighted in red. Scale bar: 50 nm.

Movie 3. Electron cryo-tomogram of GFP-Bax cluster obtained from cryo-FIB milled cells, corresponding to Figure 3I-K'. Movie through virtual slices of electron cryo-tomogram. 3D segmentation model of mitochondrion is shown as an overlay. Outer membranes in dark blue, inner membranes in light blue, and ribosomes in intermembrane space in white. Movie pauses at the virtual slice shown in Fig. 3K and K' to indicate structural features highlighted in red. Scale bar: 50 nm.

Movie 4. Electron cryo-tomogram of GFP-Bax clusters and inner membrane rupture obtained from cryo-FIB milled cells, corresponding to Figure 3L-Q'. Movie through virtual slices of electron cryo-tomogram. 3D segmentation model of mitochondrion is shown as an overlay. Outer membranes are in dark blue, inner membranes in light blue. White borders indicate end of segmentation (see Materials and Methods). Movie pauses at the virtual slice shown in Fig. 3N and N', and at the virtual slice shown in Fig. 3Q and Q' to indicate structural features highlighted in red. Scale bar: 50 nm.

Supplementary Table T1. Sample sizes from which the analyzed electron tomography data sets were generated. Counts include only samples that have contributed to the final data presented in this study. Additional samples and data have been excluded based on either one or more of the following criteria: poor

887 vitrification/sample quality, poor tilt series acquisition quality, poor tomographic
888 reconstruction, no structure of interest contained in the tomographic volume.
889

REFERENCES

Ader, N.R., and W. Kukulski. 2017. triCLEM: Combining high-precision, room temperature CLEM with cryo-fluorescence microscopy to identify very rare events. *Methods Cell Biol*. 140:303-320.

Al-Amoudi, A., D. Studer, and J. Dubochet. 2005. Cutting artefacts and cutting process in vitreous sections for cryo-electron microscopy. *J Struct Biol*. 150:109-121.

Anselmi, C., K.M. Davies, and J.D. Faraldo-Gomez. 2018. Mitochondrial ATP synthase dimers spontaneously associate due to a long-range membrane-induced force. *J Gen Physiol*. 150:763-770.

Antonsson, B., F. Conti, A. Ciavatta, S. Montessuit, S. Lewis, I. Martinou, L. Bernasconi, A. Bernard, J.J. Mermod, G. Mazzei, K. Maundrell, F. Gambale, R. Sadoul, and J.C. Martinou. 1997. Inhibition of Bax channel-forming activity by Bcl-2. *Science*. 277:370-372.

Antonsson, B., S. Montessuit, S. Lauper, R. Eskes, and J.C. Martinou. 2000. Bax oligomerization is required for channel-forming activity in liposomes and to trigger cytochrome c release from mitochondria. *The Biochem J*. 345 Pt 2:271-278.

Ayton, G.S., E. Lyman, V. Krishna, R.D. Swenson, C. Mim, V.M. Unger, and G.A. Voth. 2009. New Insights into BAR Domain-Induced Membrane Remodeling. *Biophys J*. 97:1616-1625.

Ban-Ishihara, R., T. Ishihara, N. Sasaki, K. Mihara, and N. Ishihara. 2013. Dynamics of nucleoid structure regulated by mitochondrial fission contributes to cristae

911 reformation and release of cytochrome c. *Proc Natl Acad Sci U S A*. 110:11863-
912 11868.
913 Basañez, G., A. Nechushtan, O. Drozhinin, A. Chanturiya, E. Choe, S. Tutt, K.A. Wood,
914 Y. Hsu, J. Zimmerberg, and R.J. Youle. 1999. Bax, but not Bcl-xL, decreases the
915 lifetime of planar phospholipid bilayer membranes at subnanomolar
916 concentrations. *Proc Natl Acad Sci U S A*. 96:5492-5497.
917 Bharat, T.A.M., P.C. Hoffmann, and W. Kukulski. 2018. Correlative Microscopy of
918 Vitreous Sections Provides Insights into BAR-Domain Organization In Situ.
919 *Structure*. 26:879-886.
920 Bleicken, S., M. Classen, P.V. Padmavathi, T. Ishikawa, K. Zeth, H.J. Steinhoff, and E.
921 Bordignon. 2010. Molecular details of Bax activation, oligomerization, and
922 membrane insertion. *J Biol Chem*. 285:6636-6647.
923 Bleicken, S., G. Jeschke, C. Stegmueller, R. Salvador-Gallego, A.J. García-Sáez, and
924 E. Bordignon. 2014. Structural Model of Active Bax at the Membrane. *Mol Cell*.
925 56:496-505.
926 Brouwer, J.M., D. Westphal, G. Dewson, A.Y. Robin, R.T. Uren, R. Bartolo, G.V.
927 Thompson, P.M. Colman, R.M. Kluck, and P.E. Czabotar. 2014. Bak core and
928 latch domains separate during activation, and freed core domains form
929 symmetric homodimers. *Mol Cell*. 55:938-946.
930 Cipolat, S., T. Rudka, D. Hartmann, V. Costa, S. Serneels, K. Craessaerts, K. Metzger,
931 L. Scorrano, and B. De Strooper. 2006. Mitochondrial rhomboid parl regulates

cytochrome c release during apoptosis via OPA1 dependent cristae remodeling. *Cell*. 126:163-175.

Czabotar, P.E., D. Westphal, G. Dewson, S. Ma, C. Hockings, W.D. Fairlie, E.F. Lee, S. Yao, A.Y. Robin, B.J. Smith, D.C. Huang, R.M. Kluck, J.M. Adams, and P.M. Colman. 2013. Bax crystal structures reveal how BH3 domains activate Bax and nucleate its oligomerization to induce apoptosis. *Cell*. 152:519-531.

Daum, B., A. Walter, A. Horst, H.D. Osiewacz, and W. Kühlbrandt. 2013. Age-dependent dissociation of ATP synthase dimers and loss of inner-membrane cristae in mitochondria. *Proc Natl Acad Sci U S A*. 110:15301-15306.

Davies, K.M., C. Anselmi, I. Wittig, J.D. Faraldo-Gomez, and W. Kühlbrandt. 2012. Structure of the yeast F1Fo-ATP synthase dimer and its role in shaping the mitochondrial cristae. *Proc Natl Acad Sci U S A*. 109:13602-13607.

Davies, K.M., M. Strauss, B. Daum, J.H. Kief, H.D. Osiewacz, A. Rycovska, V. Zickermann, and W. Kühlbrandt. 2011. Macromolecular organization of ATP synthase and complex I in whole mitochondria. *Proc Natl Acad Sci U S A*. 108:14121-14126.

Dewson, G., T. Kratina, H.W. Sim, H. Puthalakath, J.M. Adams, P.M. Colman, and R.M. Kluck. 2008. To trigger apoptosis, Bak exposes its BH3 domain and homodimerizes via BH3:groove interactions. *Mol Cell*. 30:369-380.

Dewson, G., S. Ma, P. Frederick, C. Hockings, I. Tan, T. Kratina, and R.M. Kluck. 2012. Bax dimerizes via a symmetric BH3:groove interface during apoptosis. *Cell Death Differ*. 19:661-670.

954 Dubochet, J., M. Adrian, J.J. Chang, J.C. Homo, J. Lepault, A.W. McDowall, and P.
955 Schultz. 1988. Cryo-electron microscopy of vitrified specimens. *Q Rev Biophys*.
956 21:129-228.
957 Edlich, F., S. Banerjee, M. Suzuki, M.M. Cleland, D. Arnoult, C. Wang, A. Neutzner, N.
958 Tjandra, and R.J. Youle. 2011. Bcl-x(L) retrotranslocates Bax from the
959 mitochondria into the cytosol. *Cell*. 145:104-116.
960 Etxebarria, A., O. Terrones, H. Yamaguchi, A. Landajuela, O. Landeta, B. Antonsson,
961 H.G. Wang, and G. Basanez. 2009. Endophilin B1/Bif-1 Stimulates BAX
962 Activation Independently from Its Capacity to Produce Large Scale Membrane
963 Morphological Rearrangements. *J Biol Chem*. 284:4200-4212.
964 Frezza, C., S. Cipolat, O. Martins de Brito, M. Micaroni, G.V. Beznoussenko, T. Rudka,
965 D. Bartoli, R.S. Polishuck, N.N. Danial, B. De Strooper, and L. Scorrano. 2006.
966 OPA1 controls apoptotic cristae remodeling independently from mitochondrial
967 fusion. *Cell*. 126:177-189.
968 Gallop, J.L., C.C. Jao, H.M. Kent, P.J. Butler, P.R. Evans, R. Langen, and H.T.
969 McMahon. 2006. Mechanism of endophilin N-BAR domain-mediated membrane
970 curvature. *EMBO J*. 25:2898-2910.
971 Griffiths, G.J., L. Dubrez, C.P. Morgan, N.A. Jones, J. Whitehouse, B.M. Corfe, C. Dive,
972 and J.A. Hickman. 1999. Cell Damage-induced Conformational Changes of the
973 Pro-Apoptotic Protein Bak In Vivo Precede the Onset of Apoptosis. *J Cell Biol*.
974 144:903-914.

975 Grosse, L., C.A. Wurm, C. Bruser, D. Neumann, D.C. Jans, and S. Jakobs. 2016. Bax
976 assembles into large ring-like structures remodeling the mitochondrial outer
977 membrane in apoptosis. *EMBO J*. 35:402-413.
978 Hagen, W.J., W. Wan, and J.A. Briggs. 2017. Implementation of a cryo-electron
979 tomography tilt-scheme optimized for high resolution subtomogram averaging. *J*
980 *Struct Biol*. 197:191-198.
981 Hahn, A., K. Parey, M. Bublitz, D.J. Mills, V. Zickermann, J. Vonck, W. Kühlbrandt, and
982 T. Meier. 2016. Structure of a Complete ATP Synthase Dimer Reveals the
983 Molecular Basis of Inner Mitochondrial Membrane Morphology. *Mol Cell*. 63:445-
984 456.
985 Hahn, A., J. Vonck, D.J. Mills, T. Meier, and W. Kühlbrandt. 2018. Structure,
986 mechanism, and regulation of the chloroplast ATP synthase. *Science*. 360.pii:
987 eaat4318
988 Han, J., P. Sabbatini, D. Perez, L. Rao, D. Modha, and E. White. 1996. The E1B 19K
989 protein blocks apoptosis by interacting with and inhibiting the p53-inducible and
990 death-promoting Bax protein. *Genes Dev*. 10:461-477.
991 Jain, A., O. Beutel, K. Ebell, S. Korneev, and J.C. Holthuis. 2017. Diverting CERT-
992 mediated ceramide transport to mitochondria triggers Bax-dependent apoptosis.
993 *J Cell Sci*. 130:360-371.
994 Jürgensmeier, J.M., Z. Xie, Q. Deveraux, L. Ellerby, D. Bredesen, and J.C. Reed. 1998.
995 Bax directly induces release of cytochrome c from isolated mitochondria. *Proc*
996 *Natl Acad Sci U S A*. 95:4997-5002.

997 Karbowski, M., Y.J. Lee, B. Gaume, S.Y. Jeong, S. Frank, A. Nechushtan, A. Santel, M.
998 Fuller, C.L. Smith, and R.J. Youle. 2002. Spatial and temporal association of Bax
999 with mitochondrial fission sites, Drp1, and Mfn2 during apoptosis. *J Cell Biol*.
1000 159:931-938.
1001 Ke, F.F.S., H.K. Vanyai, A.D. Cowan, A.R.D. Delbridge, L. Whitehead, S. Grabow, P.E.
1002 Czabotar, A.K. Voss, and A. Strasser. 2018. Embryogenesis and Adult Life in the
1003 Absence of Intrinsic Apoptosis Effectors BAX, BAK, and BOK. *Cell*. 173:1217-
1004 1230.e17.
1005 Kremer, J.R., D.N. Mastronarde, and J.R. McIntosh. 1996. Computer visualization of
1006 three-dimensional image data using IMOD. *J Struct Biol*. 116:71-76.
1007 Kühlbrandt, W. 2015. Structure and function of mitochondrial membrane protein
1008 complexes. *BMC Biol*. 13:89.
1009 Kukulski, W., M. Schorb, S. Welsch, A. Picco, M. Kaksonen, and J.A. Briggs. 2011.
1010 Correlated fluorescence and 3D electron microscopy with high sensitivity and
1011 spatial precision. *J Cell Biol*. 192:111-119.
1012 Kukulski, W., M. Schorb, S. Welsch, A. Picco, M. Kaksonen, and J.A. Briggs. 2012.
1013 Precise, correlated fluorescence microscopy and electron tomography of lowicryl
1014 sections using fluorescent fiducial markers. *Methods Cell Biol*. 111:235-257.
1015 Kuwana, T., M.R. Mackey, G. Perkins, M.H. Ellisman, M. Latterich, R. Schneiter, D.R.
1016 Green, and D.D. Newmeyer. 2002. Bid, Bax, and lipids cooperate to form
1017 supramolecular openings in the outer mitochondrial membrane. *Cell*. 111:331-
1018 342.

1019 Labi, V., and M. Erlacher. 2015. How cell death shapes cancer. *Cell Death Dis*. 6:e1675

1020 Lovell, J.F., L.P. Billen, S. Bindner, A. Shamas-Din, C. Fradin, B. Leber, and D.W.
1021 Andrews. 2008. Membrane Binding by tBid Initiates an Ordered Series of Events
1022 Culminating in Membrane Permeabilization by Bax. *Cell*. 135:1074-1084.

1023 Mahamid, J., S. Pfeffer, M. Schaffer, E. Villa, R. Danev, L.K. Cuellar, F. Forster, A.A.
1024 Hyman, J.M. Plitzko, and W. Baumeister. 2016. Visualizing the molecular
1025 sociology at the HeLa cell nuclear periphery. *Science*. 351:969-972.

1026 Marko, M., C. Hsieh, R. Schalek, J. Frank, and C. Mannella. 2007. Focused-ion-beam
1027 thinning of frozen-hydrated biological specimens for cryo-electron microscopy.
1028 *Nat Methods*. 4:215-217.

1029 Mastronarde, D.N. 2005. Automated electron microscope tomography using robust
1030 prediction of specimen movements. *J Struct Biol*. 152:36-51.

1031 McArthur, K., L.W. Whitehead, J.M. Heddleston, L. Li, B.S. Padman, V. Oorschot, N.D.
1032 Geoghegan, S. Chappaz, S. Davidson, H. San Chin, R.M. Lane, M. Dramicanin,
1033 T.L. Saunders, C. Sugiana, R. Lessene, L.D. Osellame, T.-L. Chew, G. Dewson,
1034 M. Lazarou, G. Ramm, G. Lessene, M.T. Ryan, K.L. Rogers, M.F. van Delft, and
1035 B.T. Kile. 2018. BAK/BAX macropores facilitate mitochondrial herniation and
1036 mtDNA efflux during apoptosis. *Science*. 359. pii: eaao6047.

1037 Nasu, Y., A. Benke, S. Arakawa, G.J. Yoshida, G. Kawamura, S. Manley, S. Shimizu,
1038 and T. Ozawa. 2016. In Situ Characterization of Bak Clusters Responsible for
1039 Cell Death Using Single Molecule Localization Microscopy. *Sci Rep*. 6:27505.

1040 Nechushtan, A., C.L. Smith, Y.T. Hsu, and R.J. Youle. 1999. Conformation of the Bax
1041 C-terminus regulates subcellular location and cell death. *EMBO J*. 18:2330-2341.
1042 Nechushtan, A., C.L. Smith, I. Lamensdorf, S.H. Yoon, and R.J. Youle. 2001. Bax and
1043 Bak coalesce into novel mitochondria-associated clusters during apoptosis. *J*
1044 *Cell Biol*. 153:1265-1276.
1045 Pastorino, J.G., S.T. Chen, M. Tafani, J.W. Snyder, and J.L. Farber. 1998. The
1046 overexpression of Bax produces cell death upon induction of the mitochondrial
1047 permeability transition. *J Biol Chem*. 273:7770-7775.
1048 Riley, J.S., G. Quarato, C. Cloix, J. Lopez, J. O'Prey, M. Pearson, J. Chapman, H.
1049 Sesaki, L.M. Carlin, J.F. Passos, A.P. Wheeler, A. Oberst, K.M. Ryan, and S.W.
1050 Tait. 2018. Mitochondrial inner membrane permeabilisation enables mtDNA
1051 release during apoptosis. *EMBO J*. pii: e99238
1052 Rostovtseva, T.K., H. Boukari, A. Antignani, B. Shiu, S. Banerjee, A. Neutzner, and R.J.
1053 Youle. 2009. Bax activates endophilin B1 oligomerization and lipid membrane
1054 vesiculation. *J Biol Chem*. 284:34390-34399.
1055 Salvador-Gallego, R., M. Mund, K. Cosentino, J. Schneider, J. Unsay, U. Schraermeyer,
1056 J. Engelhardt, J. Ries, and A.J. Garcia-Saez. 2016. Bax assembly into rings and
1057 arcs in apoptotic mitochondria is linked to membrane pores. *EMBO J*. 35:389-
1058 401.
1059 Schafer, B., J. Quispe, V. Choudhary, J.E. Chipuk, T.G. Ajero, H. Du, R. Schneiter, T.
1060 Kuwana, and T.D. Fox. 2009. Mitochondrial Outer Membrane Proteins Assist Bid
1061 in Bax-mediated Lipidic Pore Formation. *Mol Biol Cell*. 20:2276-2285.

1062 Schaffer, M., B.D. Engel, T. Laugks, J. Mahamid, J.M. Plitzko, and W. Baumeister.
1063 2015. Cryo-focused Ion Beam Sample Preparation for Imaging Vitreous Cells by
1064 Cryo-electron Tomography. *Bio Protoc*. 5:e1575.
1065 Schlesinger, P.H., A. Gross, X.M. Yin, K. Yamamoto, M. Saito, G. Waksman, and S.J.
1066 Korsmeyer. 1997. Comparison of the ion channel characteristics of proapoptotic
1067 BAX and antiapoptotic BCL-2. *Proc Natil Acad Sci U S A*. 94:11357-11362.
1068 Schorb, M., and J.A. Briggs. 2014. Correlated cryo-fluorescence and cryo-electron
1069 microscopy with high spatial precision and improved sensitivity. *Ultramicroscopy*.
1070 143:24-32.
1071 Scorrano, L., M. Ashiya, K. Buttle, S. Weiler, S.A. Oakes, C.A. Mannella, and S.J.
1072 Korsmeyer. 2002. A distinct pathway remodels mitochondrial cristae and
1073 mobilizes cytochrome c during apoptosis. *Dev Cell*. 2:55-67.
1074 Simunovic, M., C. Mim, T.C. Marlovits, G. Resch, V.M. Unger, and G.A. Voth. 2013.
1075 Protein-mediated transformation of lipid vesicles into tubular networks. *Biophys J*.
1076 105:711-719.
1077 Speck, S.H., C.A. Neu, M.S. Swanson, and E. Margoliash. 1983. Role of Phospholipid
1078 in the Low Affinity Reactions between Cytochrome-C and Cytochrome-Oxidase.
1079 *FEBS Lett*. 164:379-382.
1080 Srivastava, A.P., M. Luo, W. Zhou, J. Symersky, D. Bai, M.G. Chambers, J.D. Faraldo-
1081 Gómez, M. Liao, and D.M. Mueller. 2018. High-resolution cryo-EM analysis of the
1082 yeast ATP synthase in a lipid membrane. *Science*. 360. pii: eaas9699.

1083 Strauss, M., G. Hofhaus, R.R. Schröder, and W. Kühlbrandt. 2008. Dimer ribbons of
1084 ATP synthase shape the inner mitochondrial membrane. *EMBO J*. 27:1154-1160.
1085 Takahashi, Y., M. Karbowski, H. Yamaguchi, A. Kazi, J. Wu, S.M. Sebti, R.J. Youle, and
1086 H.G. Wang. 2005. Loss of Bif-1 suppresses Bax/Bak conformational change and
1087 mitochondrial apoptosis. *Mol Cell Biol*. 25:9369-9382.
1088 Uren, R.T., M. O'Hely, S. Iyer, R. Bartolo, M.X. Shi, J.M. Brouwer, A.E. Alsop, G.
1089 Dewson, and R.M. Kluck. 2017. Disordered clusters of Bak dimers rupture
1090 mitochondria during apoptosis. *Elife*. 6:e19944.
1091 Valldeperas, M., M. Wisniewska, M. Ram-On, E. Kesselman, D. Danino, T. Nylander,
1092 and J. Barauskas. 2016. Sponge Phases and Nanoparticle Dispersions in
1093 Aqueous Mixtures of Mono- and Diglycerides. *Langmuir*. 32:8650-8659.
1094 van Delft, M.F., A.H. Wei, K.D. Mason, C.J. Vandenberg, L. Chen, P.E. Czabotar, S.N.
1095 Willis, C.L. Scott, C.L. Day, S. Cory, J.M. Adams, A.W. Roberts, and D.C. Huang.
1096 2006. The BH3 mimetic ABT-737 targets selective Bcl-2 proteins and efficiently
1097 induces apoptosis via Bak/Bax if Mcl-1 is neutralized. *Cancer Cell*. 10:389-399.
1098 Vik, S.B., G. Georgevich, and R.A. Capaldi. 1981. Diphosphatidylglycerol is required for
1099 optimal activity of beef heart cytochrome c oxidase. *Proc Natl Acad Sci U S A*.
1100 78:1456-1460.
1101 Watson, M.L. 1958. Staining of Tissue Sections for Electron Microscopy with Heavy
1102 Metals. *J Biophys Biochem Cytol*. 4:475-478.
1103 Westphal, D., G. Dewson, M. Menard, P. Frederick, S. Iyer, R. Bartolo, L. Gibson, P.E.
1104 Czabotar, B.J. Smith, J.M. Adams, and R.M. Kluck. 2014. Apoptotic pore

formation is associated with in-plane insertion of Bak or Bax central helices into the mitochondrial outer membrane. *Proc Natl Acad Sci U S A*. 111:E4076-4085.

Wolf, S.G., Y. Mutsafi, T. Dadosh, T. Ilani, Z. Lansky, B. Horowitz, S. Rubin, M. Elbaum, and D. Fass. 2017. 3D visualization of mitochondrial solid-phase calcium stores in whole cells. *Elife*. 6:e29929.

Youle, R.J., and A. Strasser. 2008. The BCL-2 protein family: opposing activities that mediate cell death. *Nat Rev Mol Cell Biol*. 9:47-59.

Zhou, L., and D.C. Chang. 2008. Dynamics and structure of the Bax-Bak complex responsible for releasing mitochondrial proteins during apoptosis. *J Cell Sci*. 121:2186-2196.

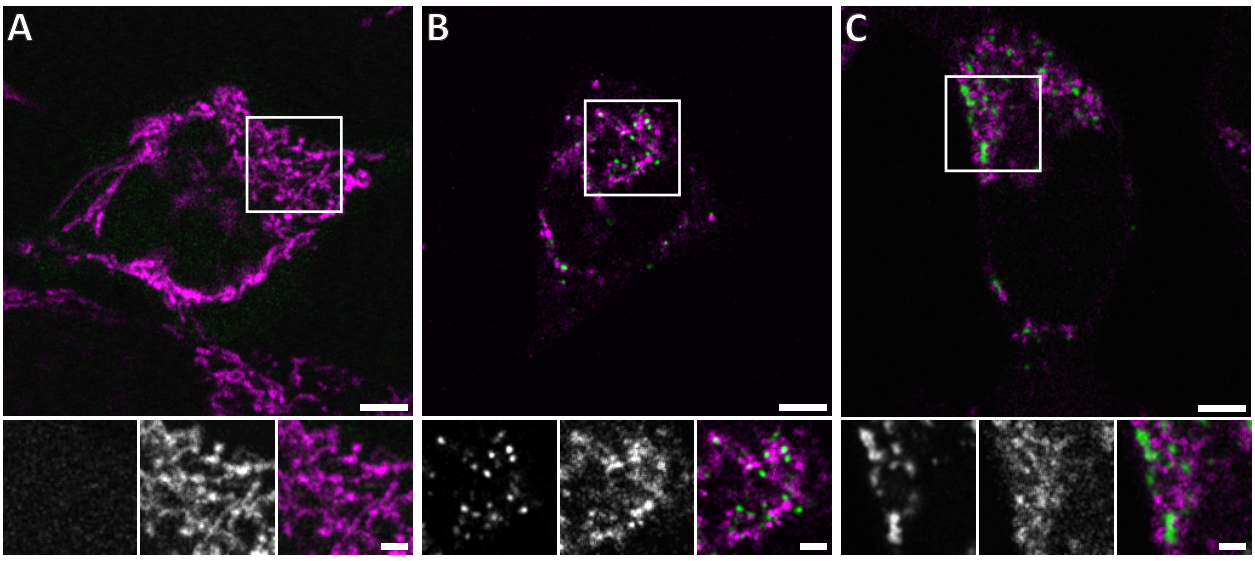

Figure 1. Live confocal fluorescence microscopy of HeLa cells overexpressing GFP-Bax. HeLa cells transfected with GFP-Bax (green) in the presence of Q-VD-OPh were imaged every 30 min, for 24 h after transfection. Cells were stained with MitoTracker Deep Red (magenta) prior to imaging. **A:** Representative cell 9 h after transfection. **B:** Representative cell 14 h after transfection, showing formation of GFP-Bax punctae. **C:** Larger clusters of GFP-Bax in a representative cell 19 h after transfection. White boxes indicate areas shown magnified below the large image. The three magnified images correspond to: GFP-Bax channel (left), MitoTracker Deep Red channel (middle), and merge (right). Scale bars: 5 μm (upper panel) and 2 μm (lower panel)

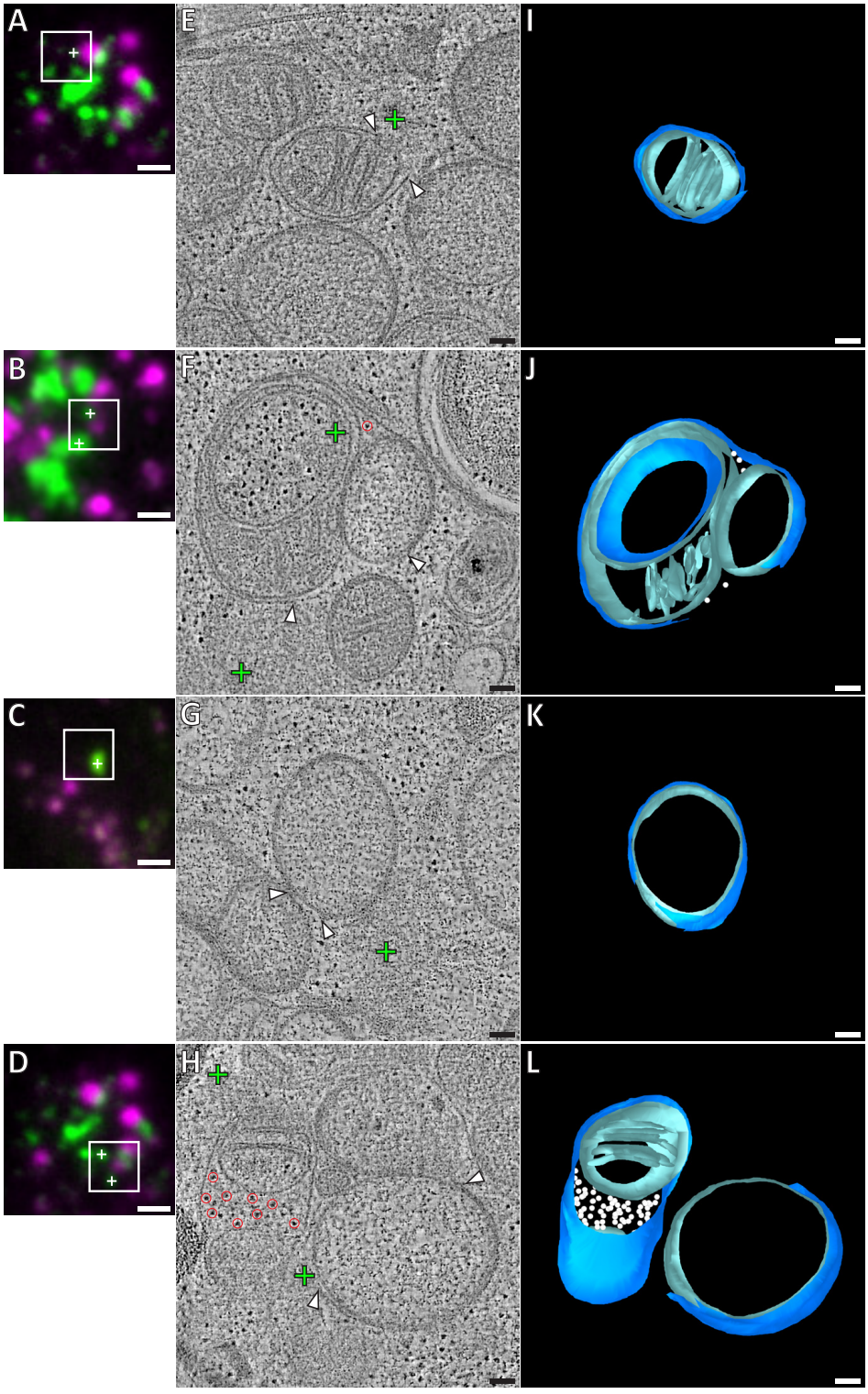

Figure 2: Correlative microscopy of resin-embedded HeLa cells overexpressing GFP-Bax. Gallery of GFP-Bax locations and the associated mitochondrial morphologies, 16 h post-transfection with GFP-Bax, in the presence of Q-VD-OPh. **A-D:** FM images of sections of resin-embedded cells. GFP-Bax (green) and MitoTracker

Deep Red (magenta). White squares indicate the field of view imaged by ET. White crosses indicate centroids of GFP-Bax signals localized in electron tomograms. **E-H:** Virtual slices from electron tomograms acquired at areas indicated by white squares in A-D, respectively. Red circles mark representative ribosomes in intermembrane space. White arrowheads indicate membrane ruptures. Green crosses indicate predicted positions of GFP-Bax signals corresponding to white crosses in fluorescence micrographs. **I-L:** 3D segmentation model of mitochondria in E-H, respectively. Outer membranes are in dark blue, inner membranes in light blue and ribosomes in the intermembrane space in white. Scale bars: 1 µm (A-D), 100 nm (E-L).

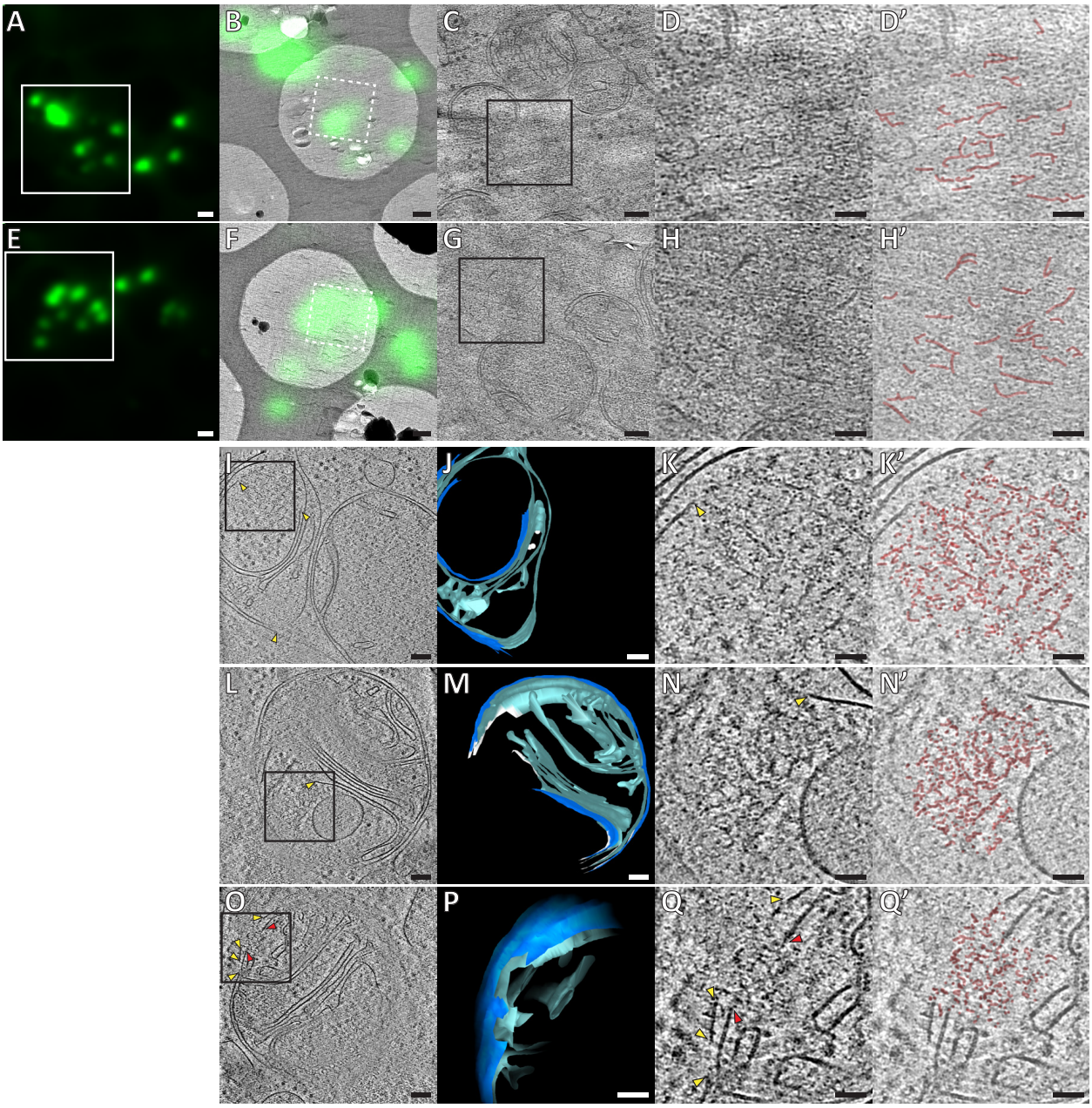

Figure 3. Ultrastructure of GFP-Bax clusters in HeLa cells visualized by cryo correlative microscopy of vitreous sections, and by cryo-ET of FIB-milled cells. A, E: Cryo-FM of vitreous sections of HeLa cells (high-pressure frozen 16 h post-transfection with GFP-Bax). GFP-Bax signal in green. White squares indicate areas shown in B and F, respectively. **B, F:** Cryo-EM overview images of areas shown in white squares in A and E, respectively. The corresponding cryo-FM images, transformed according to correlation procedure, are overlaid in green. White dashed squares indicate areas imaged by cryo-ET. **C, G:** Virtual slices through electron cryo-tomograms corresponding to white dashed squares in B and F, respectively. Black squares indicate areas magnified in D, H, respectively. **D, H:** Magnifications of virtual slices shown in C and G, respectively, areas corresponding to black squares. **D', H'**: Annotation of images

in D and H, respectively. Structural features of the GFP-Bax cluster ultrastructure are highlighted in red. **I, L, O:** Virtual slices through electron cryo-tomograms of HeLa cells (plunge-frozen 16 h post transfection with GFP-Bax), targeted by cryo-FM (see Suppl. Fig. S3) and thinned by cryo-FIB milling. Note that L and O show different virtual slices of the same mitochondrion; rotated by 180˚ around the image y-axis. Black squares indicate areas magnified in K, N and Q, respectively. Yellow and red arrowheads indicate ruptured outer and inner membranes, respectively. **J, M and P:** 3D segmentation model of mitochondria seen in I, L and O, respectively. Outer membranes are in dark blue, inner membranes in light blue, and ribosomes in intermembrane space in white (J). White borders (M) indicate end of segmentation (see Materials and Methods). Note that M and P show the same mitochondrion at different angles and magnifications. **K, N and Q:** Magnifications of virtual slices shown in I and L, respectively, areas corresponding to the black squares. Yellow and red arrowheads indicate ruptured outer and inner membranes, respectively. **K', N' and Q'**: Annotation of images in K, N and Q, respectively. Structural features of the cluster ultrastructure are highlighted in red. Scale bars: 1 µm (A, E), 500 nm (B, F), 100 nm (C, G, I, J, L, M, O, P), 50 nm (D, D' H, H' K, K', N, N', Q, Q').

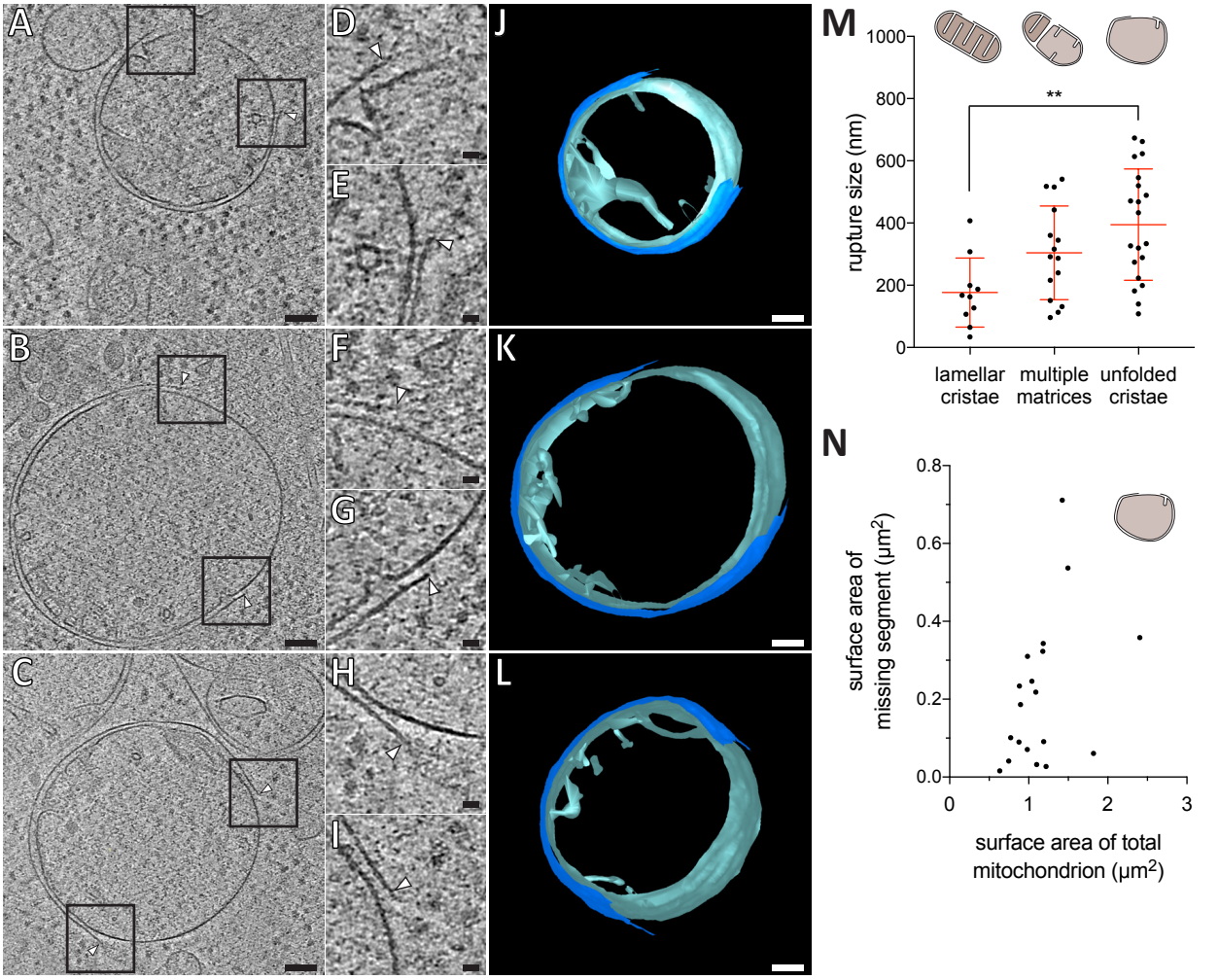

Figure 4. Mitochondrial outer membrane ruptures are accompanied by rearrangements of the inner membrane. A-C: Virtual slices through electron cryo-tomograms of HeLa cells (16 h post transfection with GFP-Bax), thinned by cryo-FIB milling. Black squares indicate areas magnified in D-I, respectively. **D-I:** Magnifications of the virtual slices shown in A-C, respectively, areas corresponding to black squares. White arrowheads indicate ruptured membranes. **J-L:** 3D segmentation model of mitochondria seen in A-C, respectively. Outer membranes are in dark blue, inner membranes in light blue. **M:** Quantification of rupture sizes, grouped according to inner membrane morphology category. Data points are from both ET of resin-embedded HeLa cells, and from cryo-ET of cryo-FIB milled HeLa cells, all 16 h post-transfection with GFP-Bax. Schematic representation of each category is shown above columns. **p=0.0024 for lamellar cristae vs. unfolded cristae. The red lines indicate the mean and the standard deviation. **N:** Surface area of the missing outer membrane segment plotted against the surface area of the total mitochondrial outer membrane, for mitochondria with mostly flattened inner membranes (indicated by schematic in upper right corner). Scale bars: 100 nm (A-C and J-L), 20 nm (D-I).

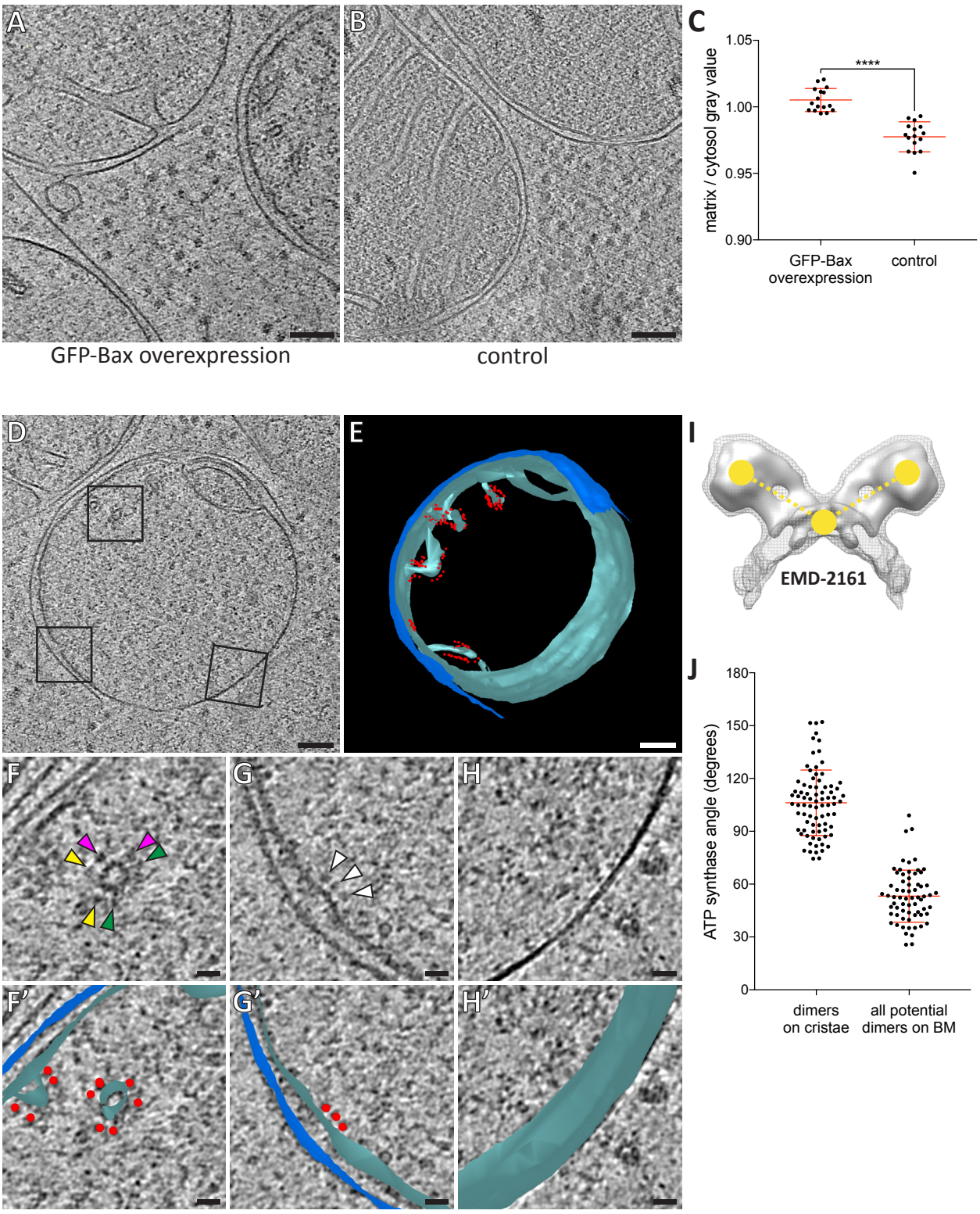

Figure 5. Dilution of the mitochondrial matrix and organization of ATP synthases visualized by cryo-ET of cryo-FIB milled HeLa cells. A: Virtual slice through an electron cryo-tomogram of a HeLa cell (16 h post-transfection with GFP-Bax) thinned by cryo-FIB milling. **B**: Virtual slice through an electron cryo-tomogram of a control HeLa

cell thinned by cryo-FIB milling, showing typical mitochondria in absence of GFP-Bax expression. **C:** Quantitative analysis of the ratio between average gray values in the matrix and average gray values in the cytosol. ****p<0.0001 for comparison between mitochondria in GFP-Bax overexpressing and control HeLa cells. The red lines indicate the mean and the standard deviation. **D:** Virtual slice through an electron cryo-tomogram of a HeLa cell (16 h post-transfection with GFP-Bax), thinned by cryo-FIB milling. Black squares indicate areas magnified in F-H. **E:** 3D segmentation model of mitochondrion seen in D. Outer membranes are in dark blue, inner membranes in light blue, and ATP synthase heads in red. **F-H:** Magnified areas of the virtual slice shown in D, corresponding to the black squares. White arrowheads indicate ATP synthase heads. Arrowheads of matching color in G denote dimers of ATP synthases. **F'-H':** Images from F-G shown with the segmentation model from E. Outer membranes are in dark blue, inner membranes in light blue, and ATP synthase heads in red. **I:** Structure of the yeast ATP synthase dimer (EMD-2161, Davies et al., 2012), to illustrate how we measured the angle enclosed by ATP synthases heads and membrane (yellow points and dashed lines) for our analysis. **J:** ATP synthase angles measured in dimers in cristae membranes, and between neighboring ATP synthases in the boundary membrane (BM). The red lines indicate the mean and the standard deviation. Scale bars: 100 nm (A, B, D, E), 20 nm (F, F', G, G', H, H').

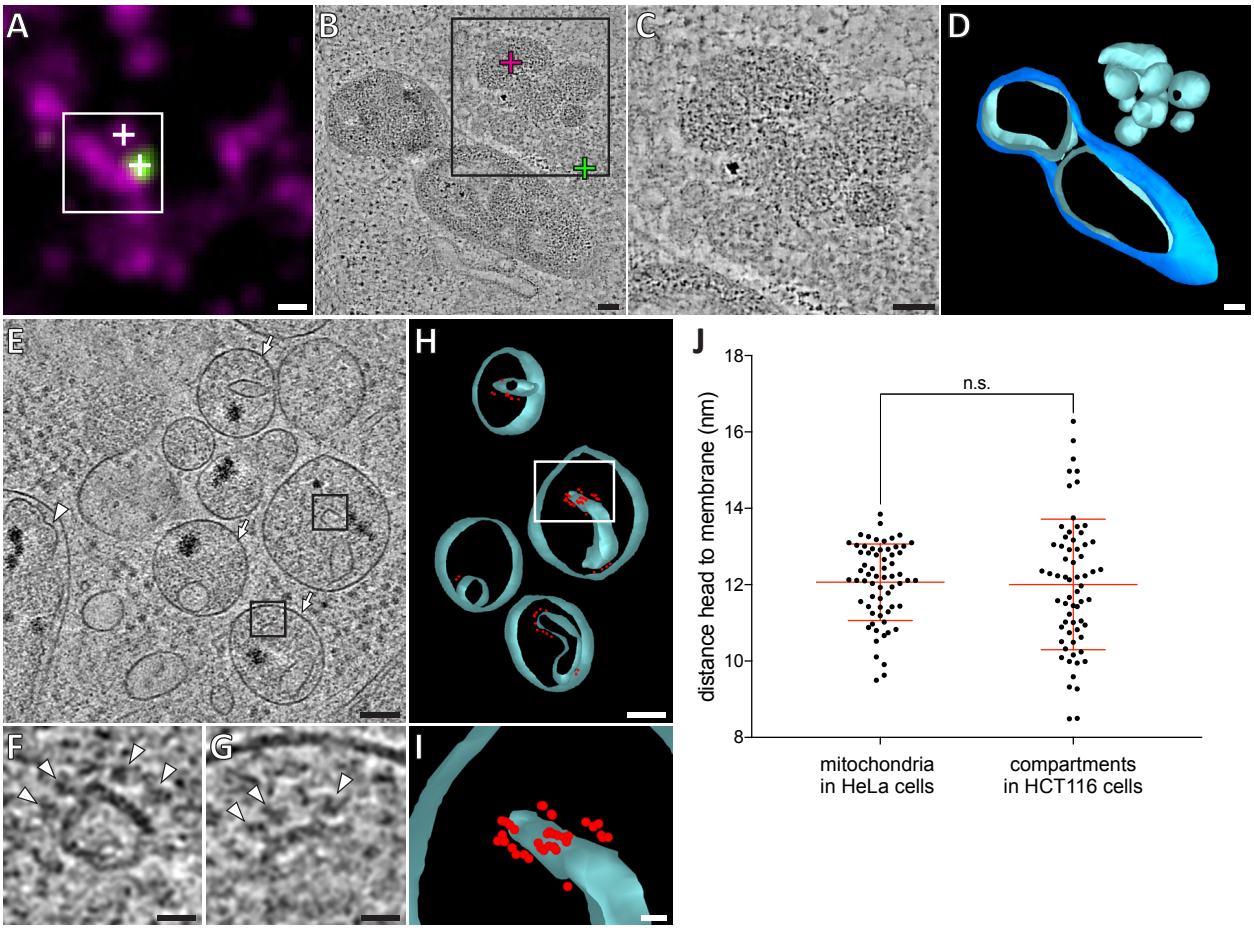

Figure 6. HCT116 cells treated with the apoptotic drug ABT-737 contain inner membrane compartments that are lacking the enclosing outer membranes. A: FM of a section of resin-embedded Bax/Bak DKO HCT116 cells stably expressing GFP-Bax, treated with ABT-737 for 3 h. GFP-Bax (green), MitoTracker Deep Red (magenta). White square indicates the field of view imaged by ET, white crosses indicate fluorescent signals of interest localized in electron tomograms. **B:** Virtual slice through an electron tomogram acquired at area indicated by the white square in A. Green and magenta crosses indicate predicted position of GFP-Bax and MitoTracker Deep Red signals, respectively. Black square indicates area magnified in C. **C:** Magnified area of the virtual slice shown in B, corresponding to the black square. The image shows an accumulation of single membrane compartments near the GFP-Bax clusters. **D:** 3D segmentation model of mitochondria and single-membrane compartments seen in B. Outer membranes are in dark blue, inner membranes in light blue. **E:** Virtual slice through an electron cryo-tomogram of a cryo-FIB milled Bax/Bak DKO HCT116 cells stably expressing GFP-Bax treated with ABT-737 3 h. Arrows indicate compartments reminiscent of mitochondrial inner membranes that appear to have no outer membrane, arrowhead indicates an inner membrane within an intact mitochondrion. **F, G:** Magnified areas of the virtual slice shown in E, corresponding to the black squares. White arrowheads indicate putative ATP synthase heads. **H:** 3D segmentation model of compartments seen in E. Membranes are in light blue, putative ATP synthase heads in

red. White box indicates magnified area in I. **I:** Magnified and rotated area from white box in H, depicting the arrangement of putative ATP synthase heads. **J:** Measured distances between head and inner membrane. Comparison between ATP synthases identified in mitochondria in HeLa cells, and putative ATP synthases in the compartments without outer membrane in HCT116 cells. The red lines indicate the mean and the standard deviation. Scale bars: 500 nm (A), 100 nm (B-E, H), 20 nm (F, G, I).

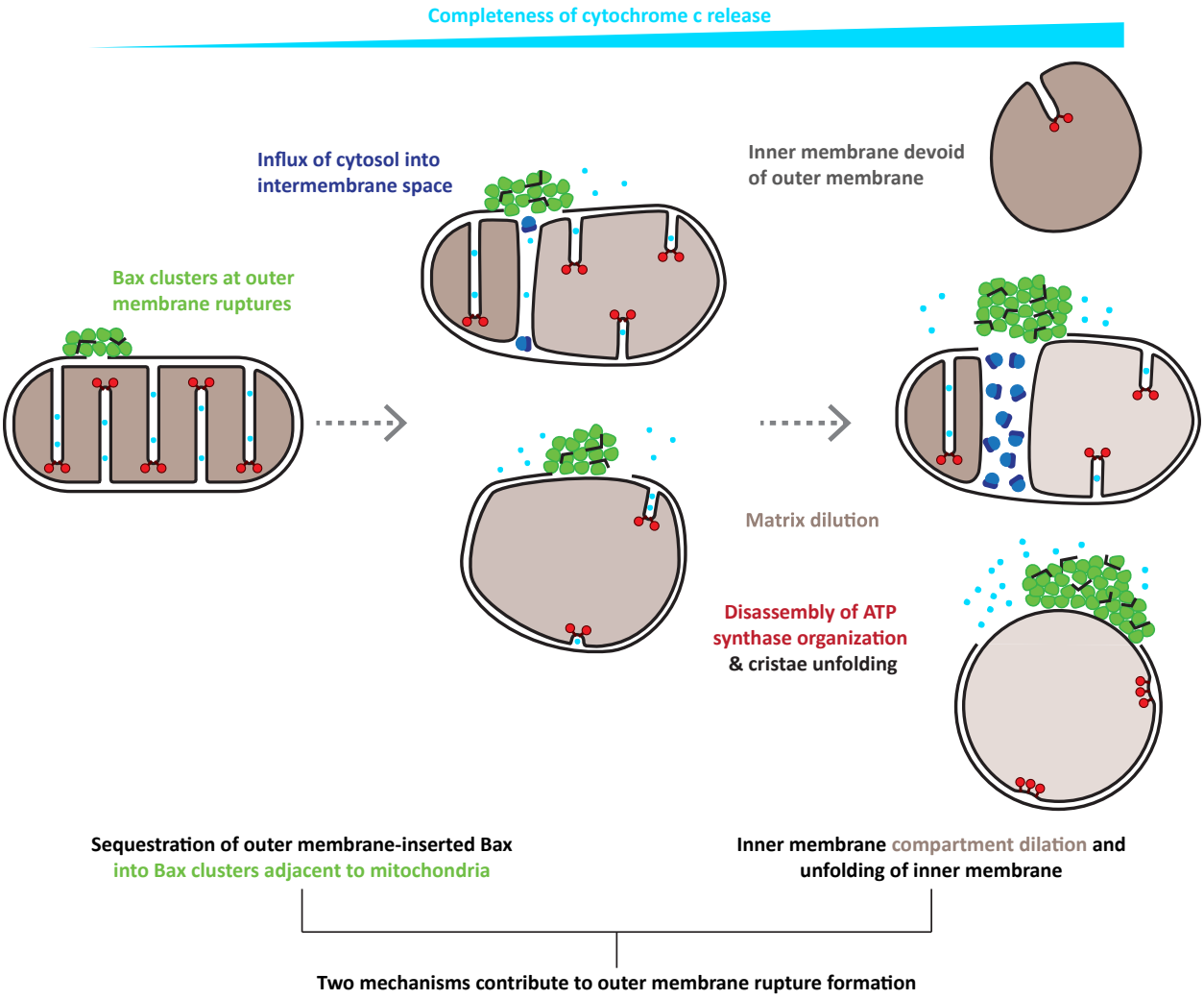

Figure 7. Model for the interplay of inner and outer membrane reorganization during Bax-mediated steps of apoptosis. Bax clusters form at outer membrane ruptures. Clusters display a higher-order organization of their components. Ruptures allow influx of ribosomes and thus mixing of cytosolic and intermembrane content. As rupture size increases, the inner membrane remodels through fragmentation and cristae unfolding. Dilution of the mitochondrial matrix likely supports dilation of the inner membrane compartment. Inner membrane reshaping is accompanied by disassembly of ATP synthase dimers into monomers and a complete clearance of ATP synthases from regions of inner membrane that are exposed to the cytosol, and that are maximally flattened. The degree of outer membrane removal varies, and is maximal in HCT116 cells, where inner membrane compartments devoid of any outer membrane can be found.

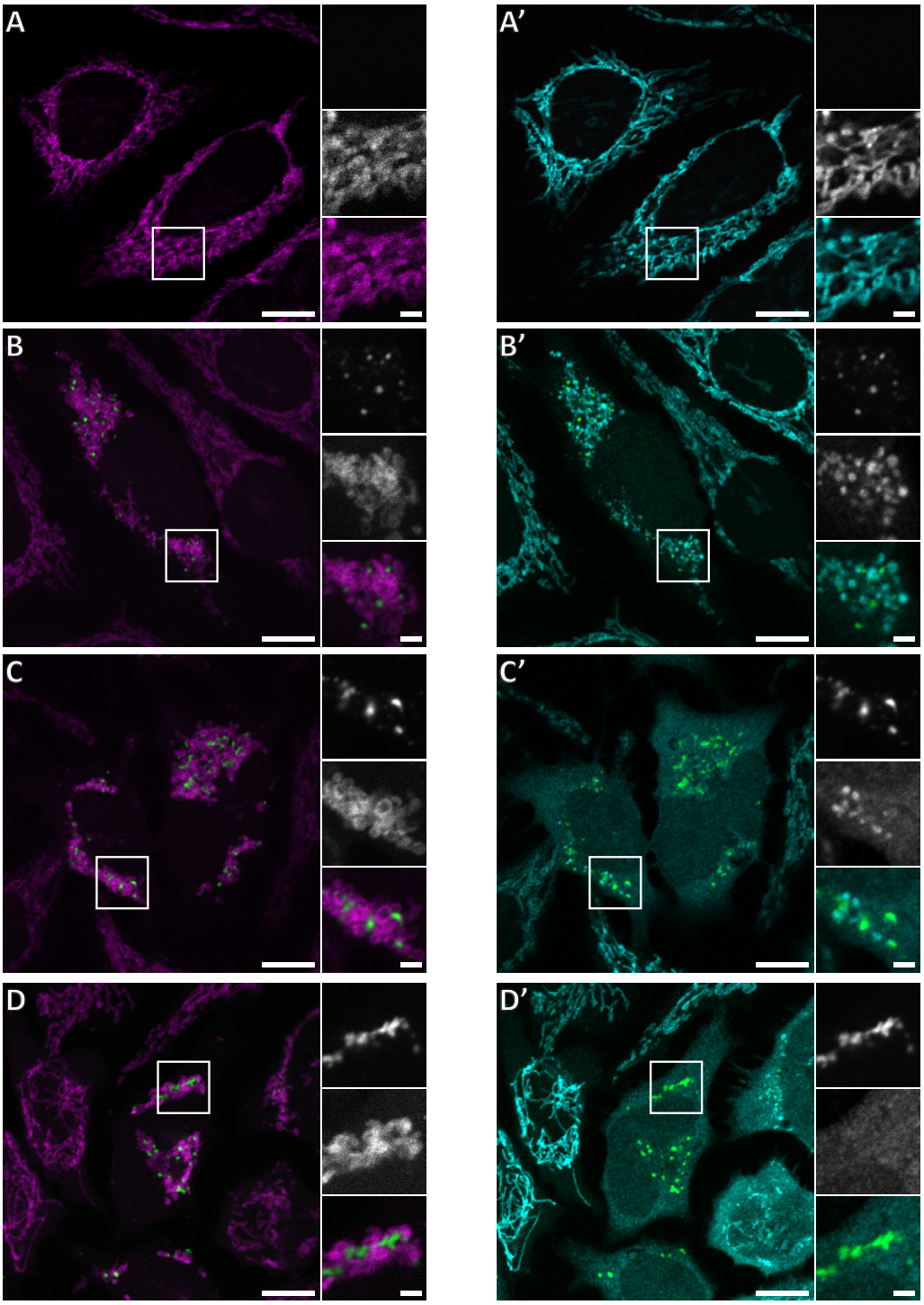

Supplementary Figure S1. Immunofluorescence of cytochrome *c* release at different stages of GFP-Bax recruitment to mitochondria. Confocal FM of fixed HeLa cells, 16 h post-transfection with GFP-Bax (green) in the presence of Q-VD-OPh. Cells were stained with antibodies for the translocase of outer membrane 20 (TOM20) (magenta) and cytochrome *c* (cyan). For better visibility, the three channels are shown as two separate merges of two channels at a time. A-D are merges of GFP-Bax (green)

with TOM20 (magenta) signals. White boxes indicate areas shown magnified to the right side of the large image. The three magnified images correspond to: GFP-Bax channel (top), TOM20 channel (middle), merge (bottom). A'-D' are merges of the GFP-Bax (green) and cytochrome *c* (cyan) signals. White boxes indicate areas shown magnified to the right side of the large image. The three magnified images correspond to: GFP-Bax channel (top), cytochrome *c* channel (middle), merge (bottom). **A, A':** Cell that does not express GFP-Bax. No release of cytochrome *c* from the mitochondria. **B, B'**: Cell that shows small punctae of GFP-Bax and displays partial release of cytochrome *c*. **C, C':** Cell that shows large clusters of GFP-Bax and displays partial release of cytochrome *c*. **D, D':** Cell that shows large clusters of GFP-Bax and displays full release of cytochrome *c* from the mitochondria into the cytosol. Scale bars are 10 μm (overview images) and 2 μm (magnified views).

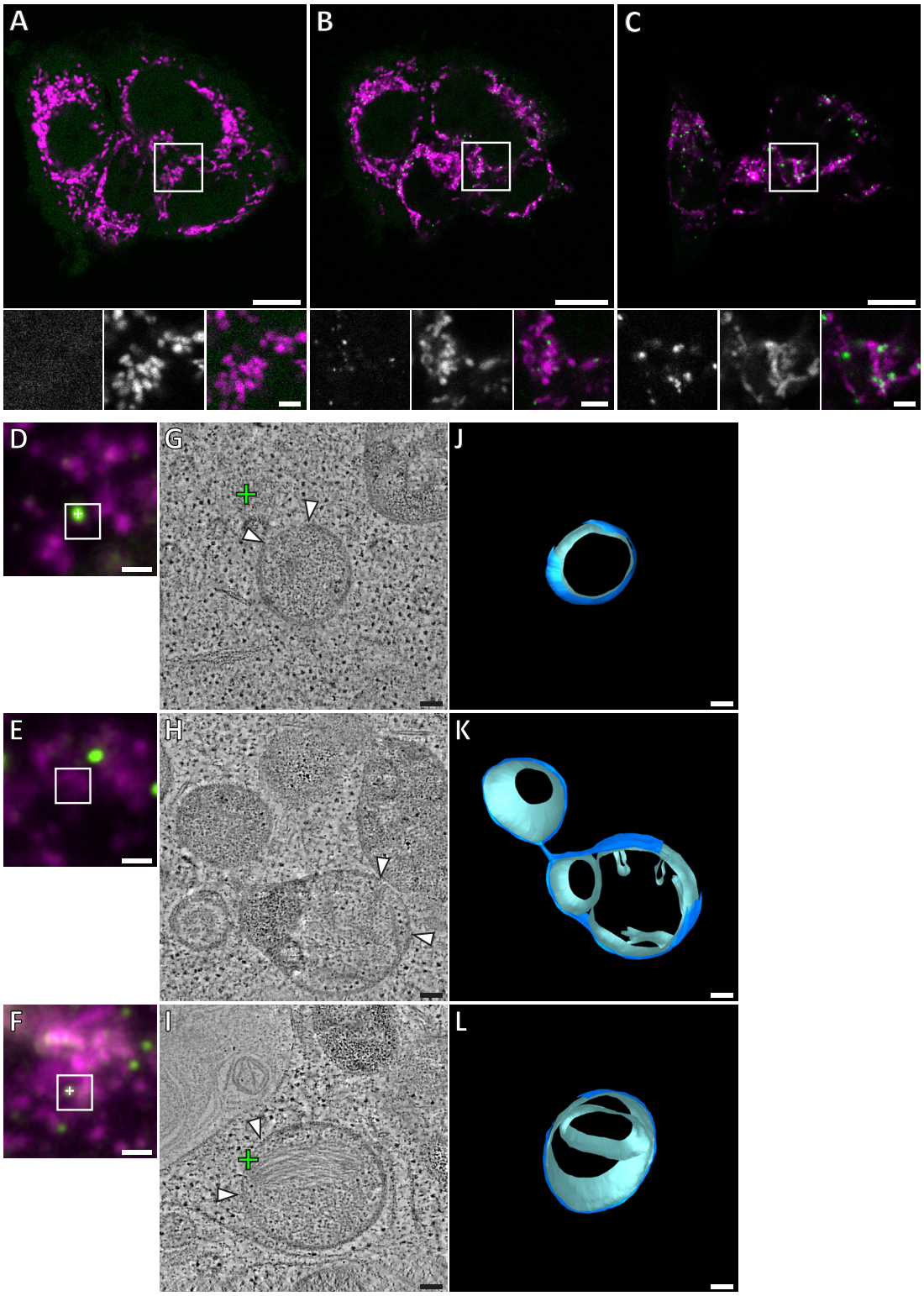

Supplementary Figure S2. Drug-induced GFP-Bax recruitment to mitochondria causes outer membrane ruptures and inner membrane rearrangement similar to those induced in HeLa cells upon GFP-Bax overexpression. Live confocal FM of Bax/Bak DKO HCT116 cells stably expressing GFP-Bax (green), treated with ABT-737

and Q-VD-OPh for 3 h. Cells were stained with MitoTracker Deep Red (magenta) prior to treatment. Cells were imaged every 30 min for 3 h after treatment. FM images shown are from **A:** 30 min, **B:** 1 h, and **C:** 2 h 30 min following treatment. White squares indicate areas shown magnified below A-C. The three magnified images correspond to: GFP-Bax channel (left), MitoTracker channel (middle), and merge (right). **D-F:** Correlative microscopy: FM image of section of resin-embedded Bax/Bak DKO HCT116 cells stably expressing GFP-Bax (green) that were treated with ABT-737 and Q-VD-OPh for 3 h. GFP-Bax (green), MitoTracker Deep Red (magenta). **G-I:** Virtual slices from electron tomograms acquired at areas indicated by white square in FM images. White arrowheads indicate ruptured membranes. Crosses indicate predicted positions of GFP-Bax signals. **J-L:** 3D segmentation model of mitochondria in G-I, respectively. Outer membranes in dark blue, inner membranes in light blue. Scale bars: 10 μm (A-C, upper panels), 2 μm (A-C, lower panels), 1 μm (D-F), 100 nm (G-L).

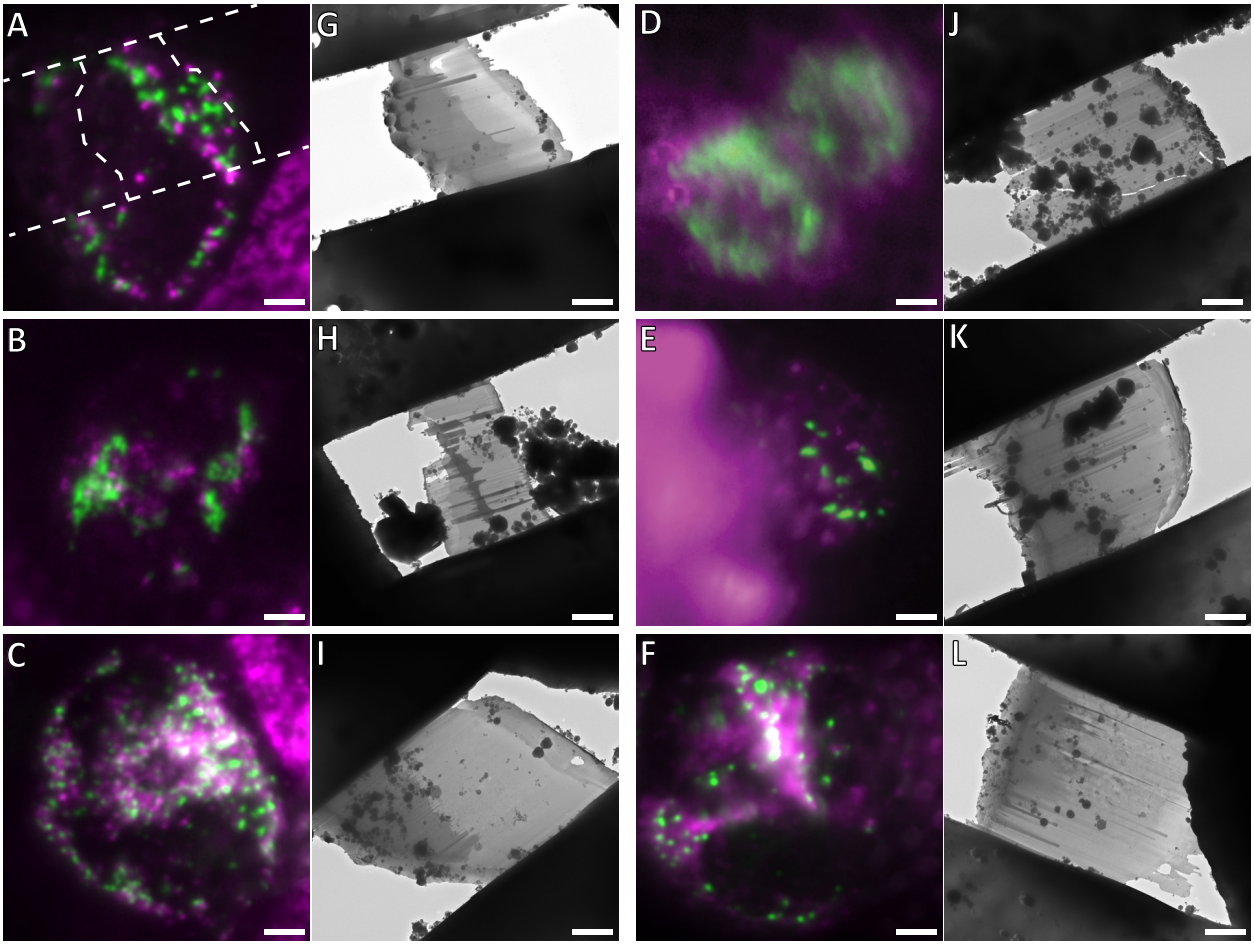

Supplementary Figure S3. Cryo-FM of mammalian cells and targeted cryo-FIB milling. Shown are all cells that were used to acquire the cryo-ET data set presented in this study. A-E and G-K are HeLa cells that were grown on EM grids and plunge-frozen 16 h after transfection with GFP-Bax. F and L show a Bax/Bak DKO HCT116 cell stably expressing GFP-Bax, that was grown on an EM grid and plunge-frozen 3 h after treatment with ABT-737. GFP-Bax (green), MitoTracker Deep Red (magenta). **A-F:** Cryo-FM of cells. Cells were selected for cryo-FIB milling based on the presence of GFP-Bax punctae. In A, the outlines of the resulting lamella are indicated by white dashed lines. **G-L:** Cryo-EM overview images of the lamellae resulting from cryo-FIB milling of the cells shown in A-F, respectively. Approximate lamella thicknesses, based on reconstruction data are: 150 nm (G), 240 nm (H), 200 nm (I), 280 nm (J), 180 nm (K), 280 nm (L). Scale bars: 5 µm (A-L).

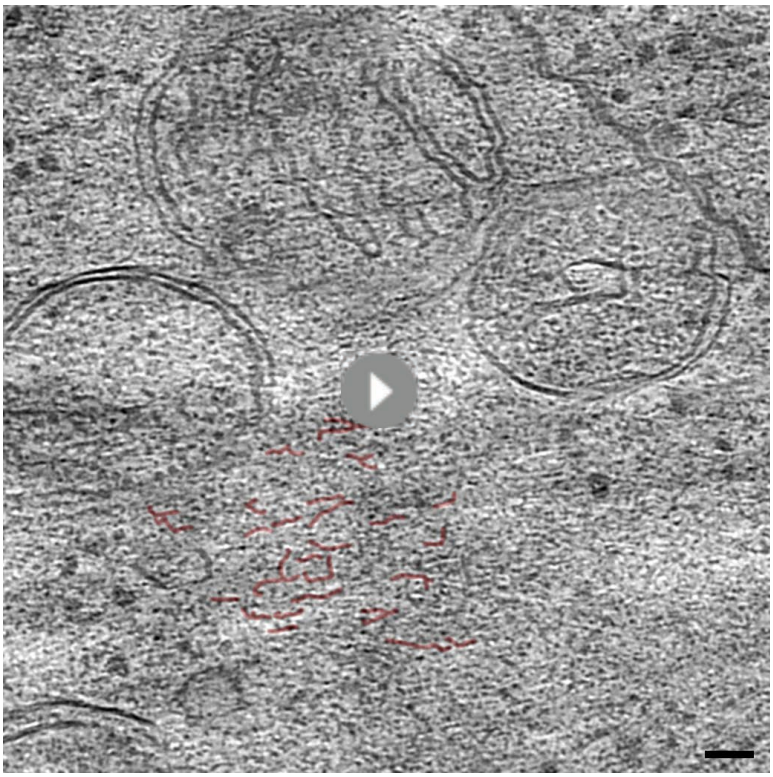

Movie 1. Electron cryo-tomogram of GFP-Bax clusters obtained by correlative microscopy of vitreous sections, corresponding to Figure 3C-D'. Movie through virtual slices of electron cryo-tomogram. Movie pauses at the virtual slice shown in Fig. 3D and D' to indicate structural features highlighted in red. Scale bar: 50 nm.

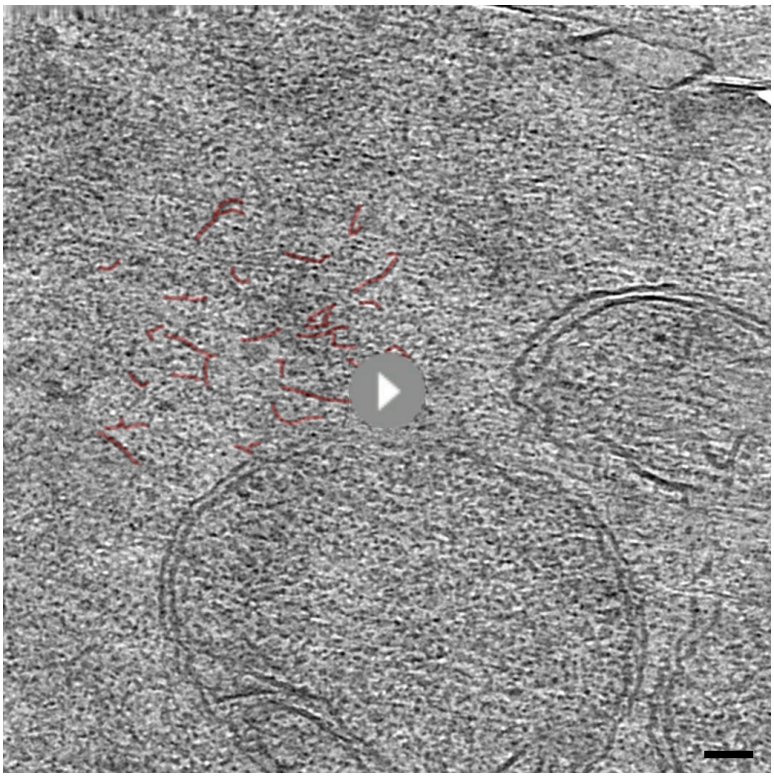

Movie 2. Electron cryo-tomogram of GFP-Bax clusters obtained by correlative microscopy of vitreous sections, corresponding to Figure 3G-H'. Movie through virtual slices of electron cryo-tomogram. Movie pauses at the virtual slice shown in Fig. 3H and H' to indicate structural features highlighted in red. Scale bar: 50 nm.

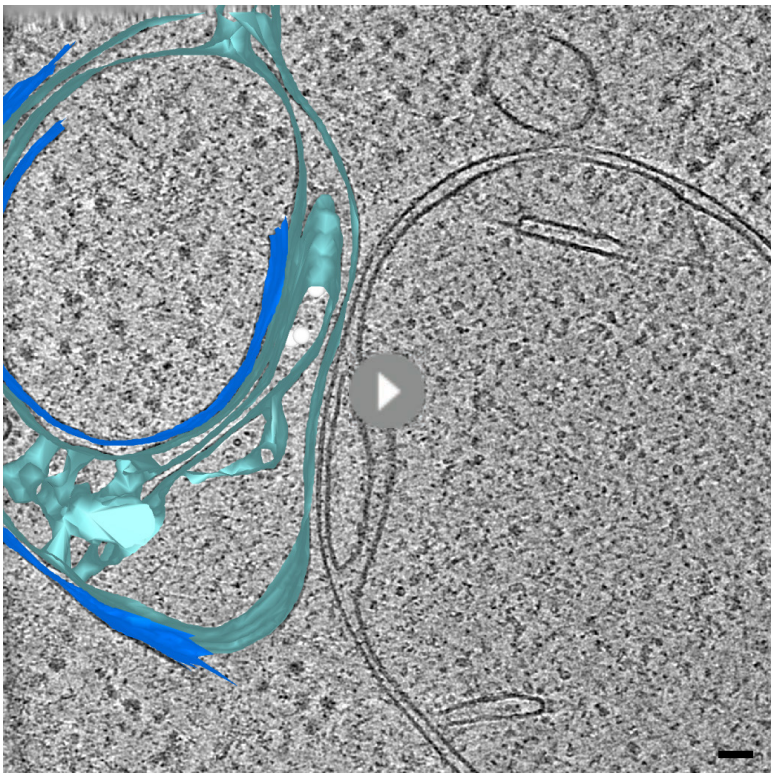

Movie 3. Electron cryo-tomogram of GFP-Bax cluster obtained from cryo-FIB milled cells, corresponding to Figure 3I-K'. Movie through virtual slices of electron cryo-tomogram. 3D segmentation model of mitochondrion is shown as an overlay. Outer membranes in dark blue, inner membranes in light blue, and ribosomes in intermembrane space in white. Movie pauses at the virtual slice shown in Fig. 3K and K' to indicate structural features highlighted in red. Scale bar: 50 nm.

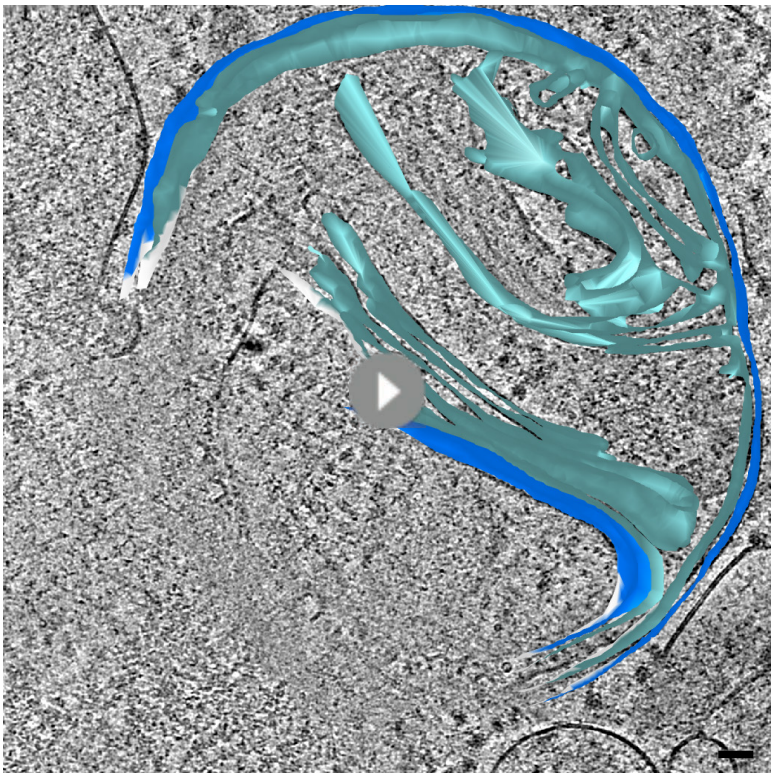

Movie 4. Electron cryo-tomogram of GFP-Bax clusters and inner membrane rupture obtained from cryo-FIB milled cells, corresponding to Figure 3L-Q'. Movie through virtual slices of electron cryo-tomogram. 3D segmentation model of mitochondrion is shown as an overlay. Outer membranes are in dark blue, inner membranes in light blue. White borders indicate end of segmentation (see Materials and Methods). Movie pauses at the virtual slice shown in Fig. 3N and N', and at the virtual slice shown in Fig. 3Q and Q' to indicate structural features highlighted in red. Scale bar: 50 nm.

electron tomography data set on:	vitrification method: high pressure freezing (HPF) or plunge freezing (PF)	number of vitrification sessions/ cell culture experiments	number of sapphires (HPF) or number of grids (PF)	number of lamellae (corresponding to number of cells)	number of electron tomograms
resin-embedded HeLa cells overexpressing GFP-Bax	HPF	1	2	n/a	51
resin-embedded Bax/Bak DKO HCT116 cells expressing GFP-Bax	HPF	1	1	n/a	35
vitreous sections of HeLa cells overexpressing GFP-Bax	HPF	1	1	n/a	5
cryo-FIB milled lamellae of HeLa cells overexpressing GFP-Bax	PF	3	5	5	8
cryo-FIB milled lamellae of control HeLa cells	PF	2	2	2	4
cryo-FIB milled lamellae of Bax/Bak DKO HCT116 cells expressing GFP-Bax	PF	1	1	1	1

Supplementary Table T1. Sample sizes from which the analyzed electron tomography data sets were generated. Counts include only samples that have contributed to the final data presented in this study. Additional samples and data have been excluded based on either one or more of the following criteria: poor vitrification/ sample quality, poor tilt series acquisition quality, poor tomographic reconstruction, no structure of interest contained in the tomographic volume.